Quantifying offshore fore-arc deformation and splay-fault slip using drowned Pleistocene shorelines, Arauco Bay, Chile

Julius Jara-Muñoz[1] (ID), Daniel Melnick[1,2] (ID), Patricio Zambrano[3] (ID), Andreas Rietbrock[4], Javiera González[5], Boris Argandoña[5], and Manfred R. Strecker[1] (ID)

[1]Institut für Erd- und Umweltwissenschaften, Universität Potsdam, Potsdam, Germany, [2]Instituto de Ciencias de la Tierra, TAQUACH, Universidad Austral de Chile, Valdivia, Chile, [3]Facultad de Ingeniería, Geología, Universidad Andres Bello, Talcahuano, Chile, [4]Department of Earth and Ocean Sciences, University of Liverpool, Liverpool, UK, [5]Hydrographic and Oceanographic Service of the Chilean Navy (SHOA), Valparaíso, Chile

Abstract Most of the deformation associated with the seismic cycle in subduction zones occurs offshore and has been therefore difficult to quantify with direct observations at millennial timescales. Here we study millennial deformation associated with an active splay-fault system in the Arauco Bay area off south central Chile. We describe hitherto unrecognized drowned shorelines using high-resolution multibeam bathymetry, geomorphic, sedimentologic, and paleontologic observations and quantify uplift rates using a Landscape Evolution Model. Along a margin-normal profile, uplift rates are 1.3 m/ka near the edge of the continental shelf, 1.5 m/ka at the emerged Santa María Island, −0.1 m/ka at the center of the Arauco Bay, and 0.3 m/ka in the mainland. The bathymetry images a complex pattern of folds and faults representing the surface expression of the crustal-scale Santa María splay-fault system. We modeled surface deformation using two different structural scenarios: deep-reaching normal faults and deep-reaching reverse faults with shallow extensional structures. Our preferred model comprises a blind reverse fault extending from 3 km depth down to the plate interface at 16 km that slips at a rate between 3.0 and 3.7 m/ka. If all the splay-fault slip occurs during every great megathrust earthquake, with a recurrence of ~150–200 years, the fault would slip ~0.5 m per event, equivalent to a magnitude ~6.4 earthquake. However, if the splay-fault slips only with a megathrust earthquake every ~1000 years, the fault would slip ~3.7 m per event, equivalent to a magnitude ~7.5 earthquake.

1. Introduction

In subduction zones, most of the deformation associated with the plate boundary megathrust both over short- and long-term timescales occurs predominantly in the offshore fore arc [e.g., *Moore*, 1979; *Savage*, 1983; *Hyndman and Wang*, 1995; *Wells et al.*, 2003]. Shortening and extension may alternate in the accretionary wedge and in areas that overlie the locked portion of the megathrust [e.g., *Wang and Hu*, 2006], where secondary structures in the upper plate, such as splay-fault systems, play a pivotal role in shaping the architecture of subduction zones [e.g.,*Barnes et al.*, 2002; *Park et al.*, 2002; *Mukoyoshi et al.*, 2006; *Moore et al.*, 2007; *Collot et al.*, 2008; *Singh et al.*, 2011; *Melnick et al.*, 2012b; *Waldhauser et al.*, 2012; *Chapman et al.*, 2014; *Hicks et al.*, 2014]. However, linking the predominantly elastic deformation associated with the plate boundary seismic cycle to the deformation recorded in the geology and geomorphology of the upper plate is not straightforward as it requires offshore observations at centennial to millennial timescales. Islands and peninsulas in the continental shelf may furnish valuable data to evaluate vertical land-level changes at various temporal scales [e.g., *Berryman*, 1993; *ten Brink et al.*, 2006; *Briggs et al.*, 2008; *Victor et al.*, 2011; *Lin et al.*, 2013; *Briggs et al.*, 2014; *Kitamura et al.*, 2014; *Wesson et al.*, 2015] but are not very common along most subduction margins. Therefore, offshore observations are required to quantify deformation rates and to link the kinematics of upper plate faults to the stick-slip cycle of the plate boundary megathrust. Drowned shorelines, geomorphic markers that have been revealed by high-resolution multibeam bathymetric surveys [*Chaytor et al.*, 2008; *Johnson et al.*, 2014; *Leclerc et al.*, 2015], may provide key information on deformation rates in offshore realms if their relation to past sea level positions and age are properly assessed. We use a multidisciplinary approach combining multibeam bathymetry, morphometric analysis, submarine observations, and landscape evolution modeling to provide a quantitative assessment of permanent deformation estimated from drowned shorelines. The study

focuses on the offshore fore-arc of the south central Chile subduction zone commonly affected by great megathrust earthquakes and characterized by complex upper plate structures.

Recent megathrust earthquakes such as the *M*9.1 Sumatra (2004), *M*8.8 Maule (2010), *M*9.2 Tohoku (2011), *M*8.2 Pisagua (2014), and *M*7.1 Araucanía (2011) events revealed that most of the plate boundary slip occurred below the offshore fore-arc [e.g., *Chlieh et al.*, 2007; *Moreno et al.*, 2010, 2012; *Satake et al.*, 2013; *Schurr et al.*, 2014; *Hicks and Rietbrock*, 2015]. Most of these earthquakes were associated with the reactivation of splay faults in the upper plate, both in offshore and onshore areas [e.g., *Kodaira et al.*, 2012; *Melnick et al.*, 2012b; *Waldhauser et al.*, 2012; *Lieser et al.*, 2014; *González et al.*, 2015]. For example, the 2010 Maule earthquake was followed by instantaneous reactivation along the Santa María fault and followed by motion along the Pichilemu fault 11 days after and a year later along the Mocha fault [*Farías et al.*, 2011; *Melnick et al.*, 2012b; *Ryder et al.*, 2012; *Hicks and Rietbrock*, 2015]. All of them are trenchward dipping structures, but of apparently different kinematics during coseismic reactivation as well as integrated at millennial timescales [e.g., *Farías et al.*, 2011; *Lange et al.*, 2012; *Melnick et al.*, 2012b; *Allmendinger et al.*, 2013; *Aron et al.*, 2013; *Melnick et al.*, 2013]. Studying the relation between the motion of such structures during great megathrust earthquakes may contribute to seismic hazard assessments and to our understanding of the buildup of topography and basin development processes in subduction zones.

The reactivation of splay faults in fore-arc settings has been discussed in the context of Coulomb wedge theory [e.g., *Dahlen et al.*, 1984; *Wang and Hu*, 2006], suggesting that faults with suitable orientation with respect to the local stress field are likely to be reactivated during megathrust earthquakes [e.g., *Sibson*, 1985; *Morris et al.*, 1996; *Loveless et al.*, 2010; *Aron et al.*, 2013]. In addition, modeling experiments have shown that the kinematics of reactivated splay faults will depend on their position with respect to the locus of coseismic slip along the plate interface, favoring normal or reverse reactivation, if most of the slip is located trenchward or landward from the branching point, respectively [*Li et al.*, 2014]. Because splay faults usually reach the seafloor at a steeper angle than the megathrust at the plate interface, their reactivation may enhance deformation locally [e.g., *Waldhauser et al.*, 2012; *Chapman et al.*, 2014] and influence the temporal evolution of tsunami waveforms [*Fukao*, 1979; *Wendt et al.*, 2009]. Considering splay faults in tsunami-hazard models requires a detailed understanding of their geometry and kinematics.

Emerged marine terraces and deformed shorelines have been long used as geomorphic markers for estimating permanent surface deformation and inferring the kinematics and slip rate of local faults and folds [e.g., *Bloom et al.*, 1974; *Lajoie*, 1986; *Anderson and Menking*, 1994; *Dickinson*, 2013]. These markers have been formed by the combined effects of tectonic uplift, wave erosion, and cliff retreat during past sea level highstands. Tectonic uplift is responsible for preserving the emerged terrace remnants forming staircase sequences if the uplift rate is higher than 0.2 mm/yr [*Pedoja et al.*, 2014], at lower rates, marine terraces may be polygenetic and record recurrent reoccupation during successive sea level highstands resulting in the development of a rasa, a wide coastal plain bounded by a steep cliff [*Paskoff*, 1977; *Regard et al.*, 2010; *Pedoja et al.*, 2014; *Melnick*, 2016]. Under favorable conditions, shorelines can also be preserved below modern sea level in areas of moderate uplift rate [e.g., *Emery*, 1958; *Sherman et al.*, 1999]. Quantitative assessments of such drowned features open new opportunities for the quantification of deformation rates orthogonal to the trench in the offshore fore arcs of subduction margins.

To bridge observations of splay-fault deformation on different timescales and to estimate the amount of permanent deformation accrued by such structures in a fore-arc setting, we analyze drowned shorelines in the Arauco Bay area of south central Chile, a region affected by recurrent megathrust earthquakes and documented splay faulting [*Moreno et al.*, 2008; *Melnick et al.*, 2012b; *Moreno et al.*, 2012; *Wesson et al.*, 2015]. We evaluate hitherto unrecognized drowned shorelines using high-resolution bathymetry and direct field observations using a remotely operated vehicle and sampling of terrace material by professional divers. We further combine our offshore assessment of deformation rates with previous estimates inferred from the deformation of onshore geomorphic markers. However, the use of drowned sea level markers for the assessment of tectonic deformation is challenging due to difficulties in collecting material for isotopic dating and performing direct on-site observations. Our objectives are threefold: (1) identify and map active structures and drowned sea level markers systematically, (2) estimate uplift rates from drowned geomorphic markers using a landscape-evolution model, and (3) assess the kinematics and associated
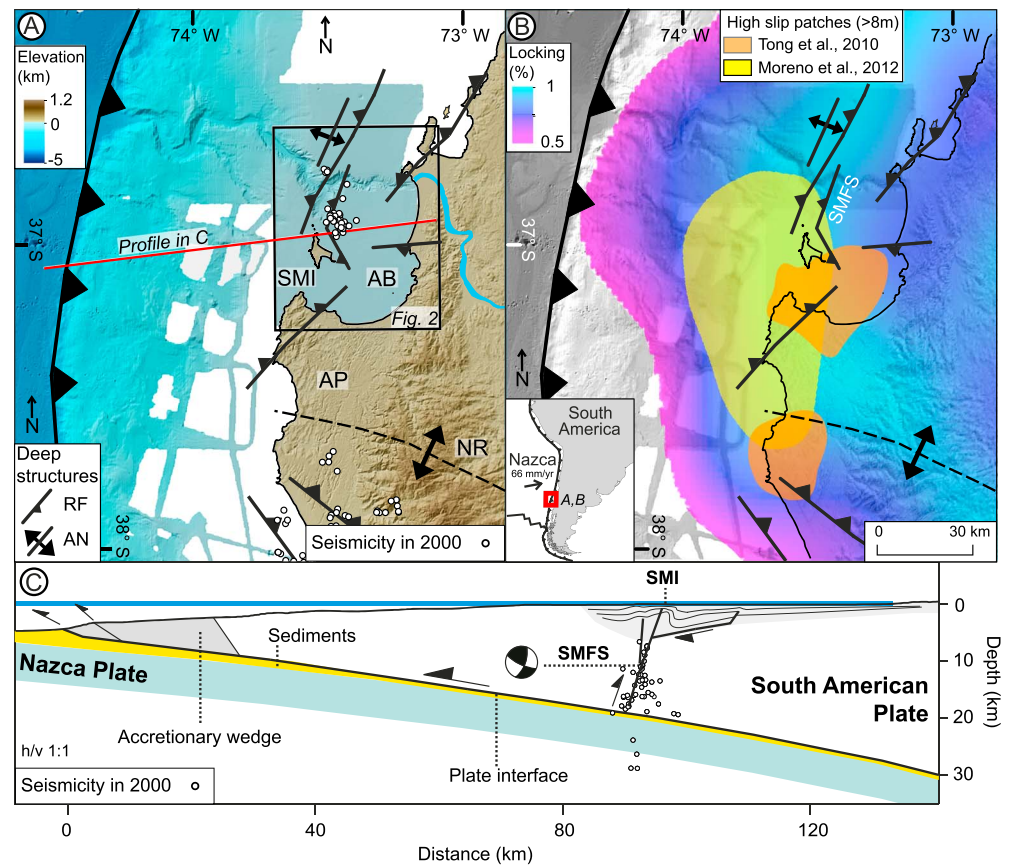
Figure 1. Regional tectonic setting. (a) Deep regional structures in the southern part of the 2010 Maule earthquake rupture zone, interpreted from seismic reflection profiles and local seismicity [*Melnick et al.*, 2006, 2012b]. SMI: Santa María Island, AB: Arauco Bay, NR: Nahuelbuta Range, RF: Reverse Fault, and AN: Anticline. (b) Seismic cycle deformation patterns in the southern part of the 2010 Maule earthquake rupture zone, high slip patches from *Moreno et al.* [2012] and *Tong et al.* [2010] and interseismic locking from *Moreno et al.* [2010]. (c) Crustal structure along profile and inferred geometry of the Santa María Fault System (SMFS) modeled in this study. Seismicity recorded by the ISSA2000 network [*Bohm et al.*, 2002], relocated using double difference method for this study. Focal mechanism of crustal *M*4.1 earthquake from *Bruhn* [2003].

deformation rates of an offshore splay-fault system. Our study reveals the offshore pattern of permanent deformation derived from drowned shorelines, suggesting slip along a trenchward dipping reverse fault rooted at the plate interface.

2. Seismotectonic and Geomorphic Setting

The Arauco Bay area is located on the continental shelf between 70 and 110 km east of the Chile trench (Figure 1a), where the ~32 Ma old Nazca Plate is subducted beneath the South American Plate at ~66 mm/yr [*Angermann et al.*, 1999]. The Arauco Bay area comprises the Arauco Bay (AB) and the Santa María Island (SMI), bounded to the south by the Arauco Peninsula and by the Bio-Bio Canyon and the Hualpén and Tumbes peninsulas to the north (Figure 2). The Arauco Peninsula and the adjacent Nahuelbuta ranges (Figure 1a) are rapidly uplifting areas (>1 mm/yr) associated with the growth of a large-scale antiform bounded by crustal reverse faults (Figure 1a) [*Kaizuka et al.*, 1973; *Melnick et al.*, 2006, 2009; *Jara-Muñoz et al.*, 2015a].

2.1. The 2010 Maule Earthquake

The Arauco Bay area is located in the southern part of the 2010 Maule earthquake rupture that affected ~500 km of the south central Chile margin (Figure 1a). This event had a moment magnitude of 8.8 and was characterized by a complex slip distribution with two main patches with peak slip of ~17 m and
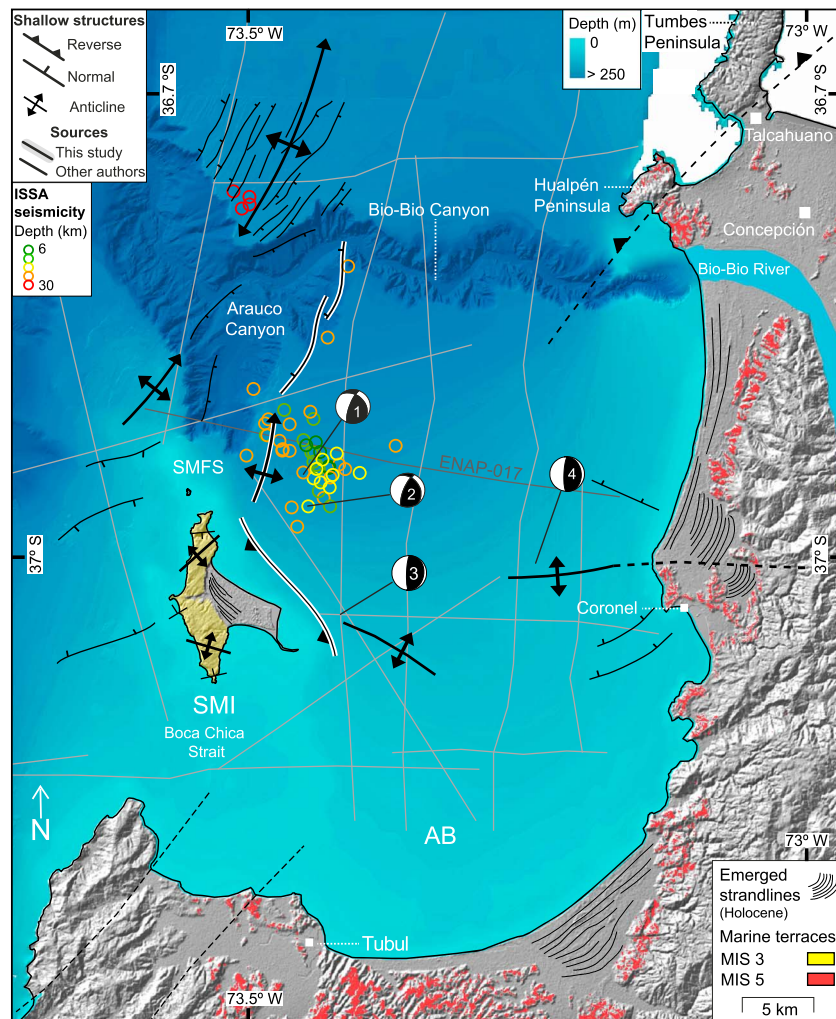
Figure 2. Shallow active structures in the Arauco Bay area interpreted from multibeam bathymetry in this study and seismic profiles in previous studies, see text for details. Patterns of uplifted Holocene strandlines and marine terraces based on *Jara-Muñoz and Melnick* [2015], *Jara-Muñoz et al.* [2015a], *Kaizuka, et al.* [1973], *Melnick et al.* [2009], *Bookhagen et al.* [2006], and *Isla et al.* [2012]. Relocated microseismicity from the ISSA2000 experiment and processed in this study, color coded by depth. Grey lines are seismic reflection profiles used by *Melnick et al.* [2012b] to map upper crustal structures. Structures identified in this study are indicated with white contour and black lines denote previously mapped structures [*Bernhardt et al.*, 2015; *Jara-Muñoz and Melnick* 2015; *Jara-Muñoz et al.*, 2015a; *Melnick et al.*, 2012b, 2006; *Melnick and Echtler*, 2006; *Wenzel et al.*, 1975]. Focal mechanisms (1) and (2) are from ISSA data [*Bruhn*, 2003] and (3) and (4) from NEIC catalogue (21 May 1990, M_w = 6.3, 11 km depth and 9 September 2010, M_w = 6.1, 16 km depth). SMFS: Santa María Fault System; SMI: Santa María Island, and AB: Arauco Bay.

~12 m at the northern and southern sectors of the rupture, respectively [*Tong et al.*, 2010; *Moreno et al.*, 2012; *Lin et al.*, 2013]. Based on GPS velocities from the decade prior to the Maule earthquake, kinematic models have revealed a heterogeneous distribution of interseismic locking that resembles the main pattern of coseismic slip distribution during the earthquake [*Moreno et al.*, 2010].

The Maule earthquake was preceded by the 1835 Concepción event (*M* > 8.5) documented by FitzRoy and Darwin [*FitzRoy et al.*, 1839; *Darwin*, 1851]. Inundation by tsunamis and coastal uplift during the 2010 and 1835 earthquakes suggests that both events were very similar [*Cisternas et al.*, 2010; *Moreno et al.*, 2010; *Melnick et al.*, 2012a]. *Wesson et al.* [2015] combined decadal- and centennial-scale observations of relative sea level changes at SMI, including both the 1835 and 2010 earthquakes, to estimate land-level changes through the entire earthquake cycle, concluding that 0.15–0.3 m of coseismic uplift in 1835 may have been stored as net permanent deformation in the crust. This is equivalent to 10–20% of net uplift at SMI and would

be equivalent to the mean uplift rate of ~1.5 mm/yr estimated over the past ~50 ka [*Jara-Muñoz and Melnick*, 2015].

2.2. Structures in the Arauco Bay Area

The scale of structural observations made in the Arauco Bay area can be divided into three groups based on their resolution and depth range: (a) crustal-scale seismicity observations reveal an aligned cluster of micro-seismicity between ~5 and ~20 km depth [*Bohm et al.*, 2002], interpreted to reflect activity along the Santa María splay-fault system (SMFS) (Figure 1c) [*Melnick et al.*, 2006]; (b) mesoscale structural observations from industry seismic reflection profiles (Figure 2) provide images of faults and syntectonic units from the upper crust between ~0.5 and ~2 km, but lacking resolution at shallow levels [*Melnick et al.*, 2006, 2012b]; and (c) local observations include uplift rates estimated from marine terraces onshore, structures mapped in coal mines on the eastern part of the AB at depths of up to ~1000 m, faults inferred from multibeam bathymetry along the flanks of the Bio-Bio Canyon and from outcrops at SMI [*Melnick et al.*, 2006; *Bernhardt et al.*, 2015; *Jara-Muñoz and Melnick*, 2015; *Jara-Muñoz et al.*, 2015a].

Structures identified using seismic reflection profiles in the Arauco Bay area comprise high-angle normal faults and reverse fault-cored anticlines affecting Cretaceous to Quaternary units [*Melnick et al.*, 2006; *Melnick and Echtler*, 2006]. The reverse faults were interpreted to result from the compressional inversion of normal faults [*Melnick and Echtler*, 2006]. Near the surface the SMFS comprises multiple strands over an area of ~30 km^2 that ultimately merge into a single master fault at greater depths as suggested by the aligned seismicity (Figure 2). North of SMI and across the Bio-Bio Canyon, a series of NNE-SSW oriented fractures, faults, and folded sedimentary rocks have been recognized using 5 m resolution multibeam bathymetry [*Bernhardt et al.*, 2015]. These features delineate the hinge of an ~13 km wide anticline associated with an ~150 m high knickzone of the canyon thalweg. In the eastern part of the bay off Coronel, WSW-ENE and NW-SE striking normal faults have been mapped in coal mines [*Wenzel et al.*, 1975] offsetting Tertiary rocks. In the adjacent onshore area, shoreline angles of the emerged marine isotope stage (MIS) 5e marine terrace record an ~10 km broad warping pattern and discrete offsets associated with a local fault of unknown kinematics [*Jara-Muñoz et al.*, 2015a]. Normal faulting affecting Plio-Quaternary units at shallow levels have been associated either with a persistent crustal tensional stress regime [*Lavenu and Cembrano*, 1999] or with shallow, bending-moment extension localized in the hinge of the fault-cored anticlines [*Melnick et al.*, 2006]. At SMI several grabens and half grabens have been documented to be associated with NE-SW and NW-SE oriented anticlines deforming late Pleistocene sediments.

2.3. Activity of the Santa María Fault System During the Seismic Cycle

The deformation rates of the SMFS have not yet been assessed, mostly due to its predominantly offshore location. At SMI, in the uplifted hanging wall block, land-level changes, and uplift rates have been estimated over decadal to millennial timescales [e.g., *Bookhagen et al.*, 2006; *Melnick et al.*, 2012b; *Wesson et al.*, 2015]. Using resurveyed nautical charts *Wesson et al.* [2015] estimated that between the 1835 and 2010 earthquakes SMI subsided about 1.6 m at a rate of 11.3 ± 4 mm/yr, which is similar to the 10.2 ± 3.4 mm/yr subsidence rate determined from campaign GPS measurements between 2004 and 2010. Subsidence has been inferred to result from interseismic locking. *Moreno et al.* [2008] used campaign GPS velocities to estimate the slip rate of the SMFS assuming homogeneous interseismic locking at full plate convergence rate, obtaining a vertical slip rate of 2.8 mm/yr and dextral slip of 6.9 mm/yr. However, these estimates are strongly dependent on the assumption of complete plate locking and have to be considered with caution.

In the year 2000 a temporary local network was deployed as part of the Integrated Seismological experiment in the Southern Andes (ISSA) with a duration of 3 months [*Bohm et al.*, 2002]. A cluster of 74 events localized in an ~90 km^2 area located 7 km northeast of SMI was recorded; the events form a NNE-SSW oriented and west dipping alignment between 0.6 km depth and the plate interface at ~15 km (Figures 1 and 2). Focal-mechanism solutions for two $M > 4$ events are compatible with reverse kinematics along a steeply dipping NNE striking fault with a minor dextral strike-slip component [*Bruhn*, 2003; *Melnick et al.*, 2006]. These seismological observations have been interpreted to reflect transient interseismic contraction along the SMFS [*Melnick et al.*, 2006]. The pulse of seismicity was apparently a transient phenomena as no events were subsequently recorded by the TIPTEQ seismic network that had been installed in this region for the duration of 1 year in 2004–2005 [*Haberland et al.*, 2009].
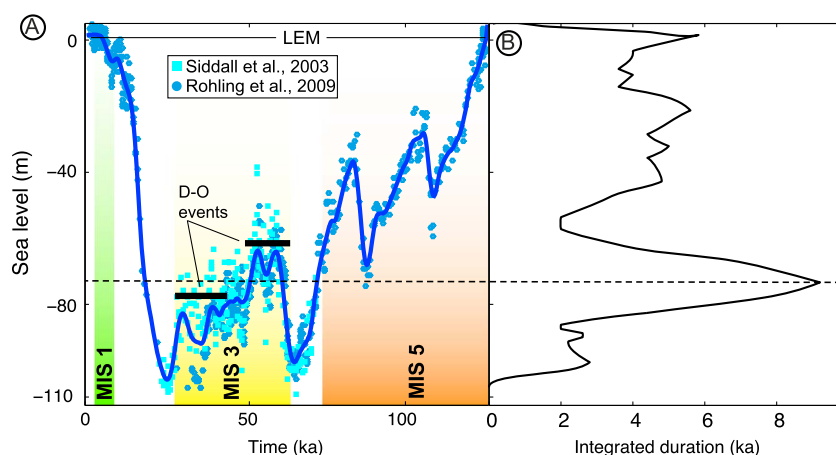
Figure 3. Sea level variations since marine isotopic stages (MIS) 5e. (a) Stack of sea level curves based on *Siddall et al.* [2003] and *Rohling et al.* [2009], see text for details. Dansgaard-Oeschger (DO) events are indicated by black thick lines. (b) Integrated sea level using 100 year time steps, note a prolonged integrated period lasting several thousand years with the sea level located at depths between 65 and 75 m bsl.

The coseismic reactivation of the SMFS was inferred during the 2010 earthquake based on field observations at SMI. Uplift estimated from displaced sessile intertidal biota, campaign GPS measurements, and synthetic aperture radar interferometry shows that during the event the SMI was uplifted between 1.6 and 2.2 m with a steep northward tilt [*Melnick et al.*, 2012b]. In addition, surface ruptures were observed along a normal fault at the northern part of the island and offshore in side-scan sonar images. Together with the overall tilt of the island these structures were interpreted to result from growth of a reverse-fault cored anticline [*Melnick et al.*, 2012b].

2.4. Marine Terraces in the Arauco Bay Area

Emerged shorelines follow the physiography of the Arauco Bay area. The younger shorelines comprise sequences of raised Holocene beach ridges reaching elevations of 8 m at SMI. The older shorelines correspond to a staircase sequence of higher marine terraces correlated with marine isotope stage (MIS) 3, 5, 7, and 9 [*Kaizuka et al.*, 1973; *Melnick et al.*, 2009; *Jara-Muñoz et al.*, 2015a] (Figure 2).

The MIS 1 is represented by sequences of parallel Holocene strandlines surrounding the Arauco Bay (Figure 2). Some of these strandlines were dated at SMI and Coronel using optically stimulated luminescence and radiocarbon dating, to between 1.8 and 4.3 ka [*Bookhagen et al.*, 2006; *Isla et al.*, 2012]. *Bookhagen et al.* [2006] proposed that strandlines at SMI have emerged as a result of recurrent coseismic uplift during megathrust earthquakes at a mean uplift rate of 2.3 ± 0.2 m/ka, which is slightly higher than the 1.5 ± 0.3 m/ka uplift rate estimated from MIS 3 deposits [e.g., *Jara-Muñoz and Melnick*, 2015]. Furthermore, the mean recurrence of strandline-forming events of ~180 years obtained by *Bookhagen et al.* [2006] is very similar to 175 years that separated the 1835 and 2010 earthquakes, suggesting coseismic uplift as a possible mechanism to explain long-term land-level changes and emergence of the island.

SMI is capped by the Santa María Formation, which consists of several sequences of beach deposits and paleosol horizons deposited during MIS 3 [*Melnick et al.*, 2006; *Jara-Muñoz and Melnick*, 2015]. MIS 3 was a period of low-amplitude climatic variability between 60 and 25 ka (Figure 3a) [*Imbrie et al.*, 1984; *Shackleton*, 2000; *Swann et al.*, 2005], characterized by a relatively stable sea level at 65 to 75 m below sea level (bsl) that lasted for ~9 ka (Figure 3b). This period comprises two episodes of subordinate sea level fluctuations associated with Dansgaard-Oeschger warming events (DO events) at −60 and 90 m bsl [e.g., *Bloom et al.*, 1974; *Chappell*, 1974; *Cabioch and Ayliffe*, 2001; *Arz et al.*, 2007; *Siddall et al.*, 2008]. By correlating these DO events with the sequence of shore environments identified in the Santa María Formation, *Jara-Muñoz and Melnick* [2015] estimated and uplift rate of 1.5 ± 0.3 m/ka at SMI.

MIS 5 terraces have been dated using infrared stimulated luminescence and cosmogenic radionuclides with ages defining the substages MIS 5a and 5e [*Melnick et al.*, 2009; *Jara-Muñoz et al.*, 2015a]. The MIS 5e terrace level reaches ~200 m at the center of the Arauco Peninsula, implying an uplift rate of 1.6 m/ka and

progressively decreasing in elevation northward to between 55 and 75 m at Coronel (Figure 2); here uplift rates vary between 0.4 and 0.6 m/ka [*Jara-Muñoz et al.*, 2015a].

3. Methods

To adequately assess deformation rates using geomorphic markers, it is first necessary to elucidate their origin and relation to past sea level positions. In this study, we first use morphometric analysis of high-resolution bathymetry, field observations from dives using a remotely operated vehicle (ROV), and sedimentologic as well as paleontologic analyses of samples collected from the seafloor to document and characterize drowned shorelines in the Arauco Bay area. After corroborating their origin, we use the shorelines to estimate uplift rates by means of a Landscape Evolution Model; these uplift rates are then incorporated in elastic dislocation models to calculate slip rates of a crustal splay-fault system.

3.1. High-Resolution Bathymetry

New generation high-resolution bathymetry allows mapping submarine geomorphic features with unprecedented detail [e.g., *Beaman et al.*, 2011; *Luján et al.*, 2011]. In this study, we use ~2000 km^2 of metric resolution bathymetry, 2 and 5 m horizontal resolution (Figures 4a and 4b), surveyed by the USS Pathfinder in the frame of a collaboration project between the Naval Oceanographic Office of the United States and the Servicio Hidrográfico y Oceanográfico de la Armada de Chile (SHOA), to produce new nautical charts after the 2010 Maule earthquake. The survey used a hull-mounted Simrad EM710 echosounder operating between 70 and 100 kHz, and the data were processed at SHOA using the CARIS, HIPS, and SIPS 7.1 software packages [*González-Acuña and Arroyo-Suarez*, 2013]. Point clouds were referred to a mean sea level datum using tide gauges and onshore topographic benchmarks and gridded at 2 m for shallow regions and 5 m for the deeper parts (>90 m bsl) (Figures 1, 2, and 4). For visualization purposes, the areas immediately adjacent to the coast, not surveyed by the USS Pathfinder, were filled with interpolated soundings available from digital nautical charts [*Servicio Hidrográfico y Oceanográfico de la Armada de Chile*, 2004] in a 20 m grid and the surveys of *Wesson et al.* [2015] (Figure 2) in a 4 m grid. Only the high-resolution multibeam swath bathymetry data were used for the morphometric analyses.

3.2. Morphometric Analysis

We use the bathymetric Surface Classification Model (SCM) to semiautomatically map remnants of paleoplatforms and paleocliffs in submarine landscapes. This method is based on *Bowles and Cowgill* [2012] and focuses on isolating rough and steep areas that may represent erosion features (Figures 4d and 4e). The model uses a combination of slope and roughness, the former defined as the standard deviation of the slope [*Frankel and Dolan*, 2007]. The analysis was performed only for depths above 140 m bsl. The SCM is defined by linearly combining ranges of slope (SLP) and surface roughness as follows:

$$SCM = \left(\frac{SLP}{max(SLP)} \times 0.5\right) + \left(\frac{std(SLP)}{max(std(SLP))} \times 0.5\right).$$

We tested several ranges of roughness and slopes to isolate rough patches from the rest of the bathymetry by analyzing frequency distributions and isolating the values above the 95th percentile of each distribution, equivalent to >1.2° for slope and >2 for roughness (Figure 4c). Roughness and slope were then normalized and linearly combined defining high-roughness patches for SCM values higher than 0, the isolated patches were manually corrected by removing false-positive classifications such as shipwrecks and survey noise. Finally, the bathymetric grid was clipped with the patches of high roughness from the SCM for further analysis (Figure 4b).

We studied 61 swath profiles of 300 m width oriented perpendicular to the trace of the high-roughness patches identified by the SCM (Figure 4b). In emerged marine terraces, the intersection between the paleocliff and paleoplatform defines the shoreline angle, a geomorphic marker that indicates the position of sea level at the moment of marine terrace formation [e.g., *Lajoie*, 1986; *Jara-Muñoz et al.*, 2015b]; however, the morphology of submerged erosive features in the Arauco Bay area differs from the typical paleocliff morphology of emerged marine terraces. To localize the shoreline angle on swath profiles, we fitted linear and exponential regressions, and then by intersecting their extrapolations, we find the location of the shoreline angle. Error estimations are obtained by intersecting the 2σ confidence intervals of each regression (Figure 5b).
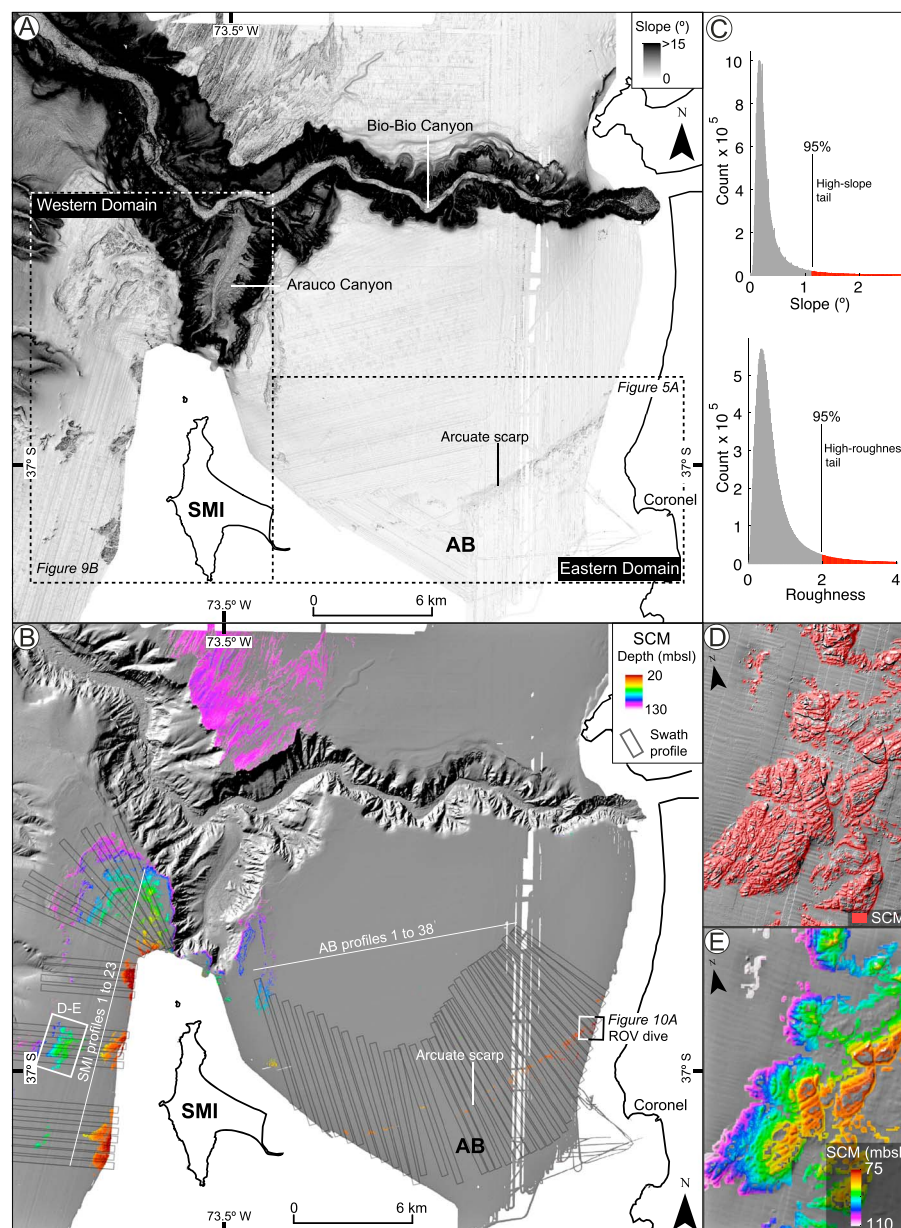
Figure 4. Extent of multibeam bathymetry used in this study and results of regional morphometric analysis. (a) Slope map of the Arauco Bay area indicating extent of the western domain centered at the Santa María Island (SMI) and the eastern domain centered at the Arauco Bay (AB). (b) Shaded bathymetry and high-roughness patches identified using the Surface Classification Model (SCM) color coded by depth. Note high-roughness clusters within the western domain and along the arcuate scarp of the eastern domain. Boxes show location of the 61 analyzed swath profiles. (c) Histograms of slope and roughness used to calibrate the SCM, red areas indicate selected ranges. (d) Example of SCM enclosing a drowned bedrock outcrop showing the extent of the mask. (e) Bathymetry pixels enclosed within the mask are color coded by depth. (See text for details.)

3.3. Submarine Imaging and Sampling

To enhance the interpretations and mapping based on high-resolution bathymetry, we selected a shallow area to perform in situ observations and sampling. The area was located in the AB, 5 km from the coastline and 7 km north of Coronel (location in Figures 4b and 5a). We used a ROV to explore an ~70 m long track along the edge of a drowned cliff obtaining video and still images, which we used to select a sediment sampling site. The sampling was carried out by professional divers who collected cobbles from the base of
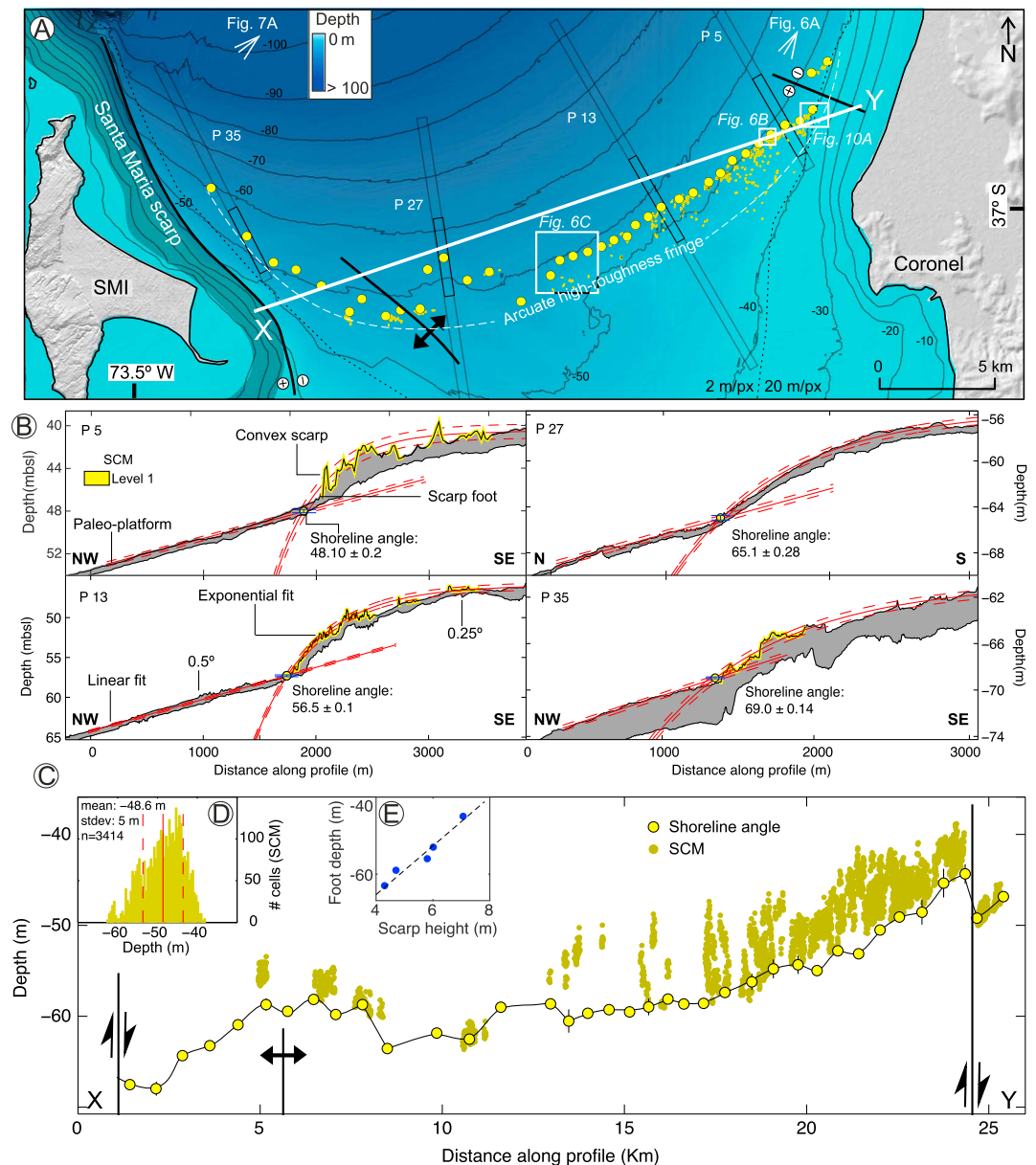
Figure 5. Morphology and structures along the eastern domain. (a) Bathymetric map indicating locations of shoreline angles (yellow dots) and high-roughness zones determined with the SCM (yellow patches). Location of swath profiles in Figure 5b are indicated by long black boxes. (b) Analysis of swath profiles using the intersection of linear and exponential regressions to find the position of shoreline angles, denoted by blue circles. (c) Profile showing distribution of the high-roughness fringe and shoreline angles, highlighting position of inferred active faults. (d) Histogram of SCM depths. (e) Relation between scarp height and cliff foot depth.

a paleocliff and sand from the flat area adjacent to its base. We study the textural and morphological characteristics of sediment samples to identify the mode of transport and energy of the depositional environment. We compare the sedimentological signature of these samples with those of active coastal environments from SMI [*Jara-Muñoz and Melnick*, 2015]. In addition, we studied pebbles and cobbles recovered from the AB using close range photogrammetry to analyze fossil bioerosion and impact marks that can provide relevant information about paleoecological and paleoenvironmental conditions [e.g., *Pleydell and Jones*, 1988; *Perry*, 1996; *Bourke et al.*, 2007]. This information was used to elucidate the origin of these features and their link with past sea level positions. (Details on the methods and results can be found in supporting information S1 and Figure S8.

3.4. Estimating Uplift Rates Using a Landscape Evolution Model

We used a Landscape Evolution Model (LEM) to simulate the development of wave-cut marine terraces and compared the results systematically with bathymetric swath profiles to estimate local uplift rates. At wave-dominated coastal systems LEMs have been used to study the development of marine landscapes under sea level variations and uplift, simulating various processes responsible for generating and dismantling the geomorphic expression of marine terraces including coral growth, sediment transport and deposition, cliff retreat, cliff diffusion, and fluvial incision [e.g., *Hanks et al.*, 1984; *Anderson et al.*, 1999; *Storms and Swift*, 2003; *Nakamura and Nakamori*, 2007; *Refice et al.*, 2012; *Thébaudeau et al.*, 2013; *Shikakura*, 2014; *Melnick*, 2016]. The LEM developed in this study is based on the wave erosion and dissipation model of *Anderson et al.* [1999], based on *Sunamura* [1992]. The model simulates the formation of wave-cut terraces under an oscillating sea level and constant uplift rate. *Melnick* [2016] applied this model to estimate uplift rates along the central Andean coast. Here we modified the model to use drowned shorelines by considering the width of the platform (as well as the depth) in the efficiency of energy dissipation, as suggested by *Bradley* [1958] and *Komar* [1998]. (Details on the methods and results can be found in the supporting information S1 and Figures S1–S4.)

The bathymetry of drowned shorelines was compared with the LEM results to determine local uplift rates. The initial model geometry consists of a linear synthetic slope scaled using the maximum and minimum depths along the length of each swath profile. In order to find the best fitting model, we tie the pattern of modeled terraces using the shoreline angle determined from the swath profiles. The horizontal scale between the LEM and each swath profile was adjusted by collocating both shoreline angles at the LEM time of formation (T). The best fitting initial erosion rate ($E0$) and uplift rate (Ur) are obtained by minimizing the root-mean-square (RMS), where n is the number of elements, Z_{obs} is the observed bathymetry, and Z_{LEM} the modeled depth profiles.

$$\text{RMS} = \sqrt{\frac{\sum (Z_{LEM} - Z_{obs})^2}{n}}.$$

H is the shoreline angle depth in meters and σH is given by the sum of vertical errors:

$$\sigma H = \sqrt{Se^2 + Sle^2 + \text{RMS}^2}$$

and include the 5 m uncertainty in absolute sea level (Sle) [*Rohling et al.*, 2009], error estimates of the shoreline angle elevations (Se), and the RMS from the LEM. Then, the standard error (S) is calculated using the following relation [*Gallen et al.*, 2014]:

$$S = \sqrt{\left(\frac{\sigma H}{H}\right)^2 + \left(\frac{\sigma T}{T}\right)^2},$$

where (σT) is an arbitrary 5 ka error for sea level correlations.

3.5. Double-Difference Relocation of Crustal Seismicity

For our analysis we use data from the ISSA temporary local seismic network that was deployed in the region for 3 months [*Bohm et al.*, 2002]. Based on the initial 1-D locations of *Bohm et al.* [2002], we selected 52 earthquakes with manually picked arrival times of P and S waves located close to SMI for the analysis. Following *Rietbrock and Waldhauser* [2004], we also estimate relative arrival times based on cross-correlation analysis in a 2.56 s time window around the P and S wave train to increase location accuracy. To study the internal seismicity structure, we use the double-difference (DD) hypoDD [*Waldhauser and Ellsworth*, 2000; *Waldhauser*, 2001] to mitigate influences of the velocity structure and the associated path effects on the earthquake locations. For the relocation we use the 1-D velocity model of *Bohm et al.* [2002]. Relative location errors are less than 50 m in all coordinate directions.

4. Results

4.1. Submarine Geomorphology of the Arauco Bay Area

The Arauco Bay area comprises two domains characterized by different morphology and depth distribution of shoreline angles and high-roughness areas identified by the SCM: an eastern domain, centered at the AB
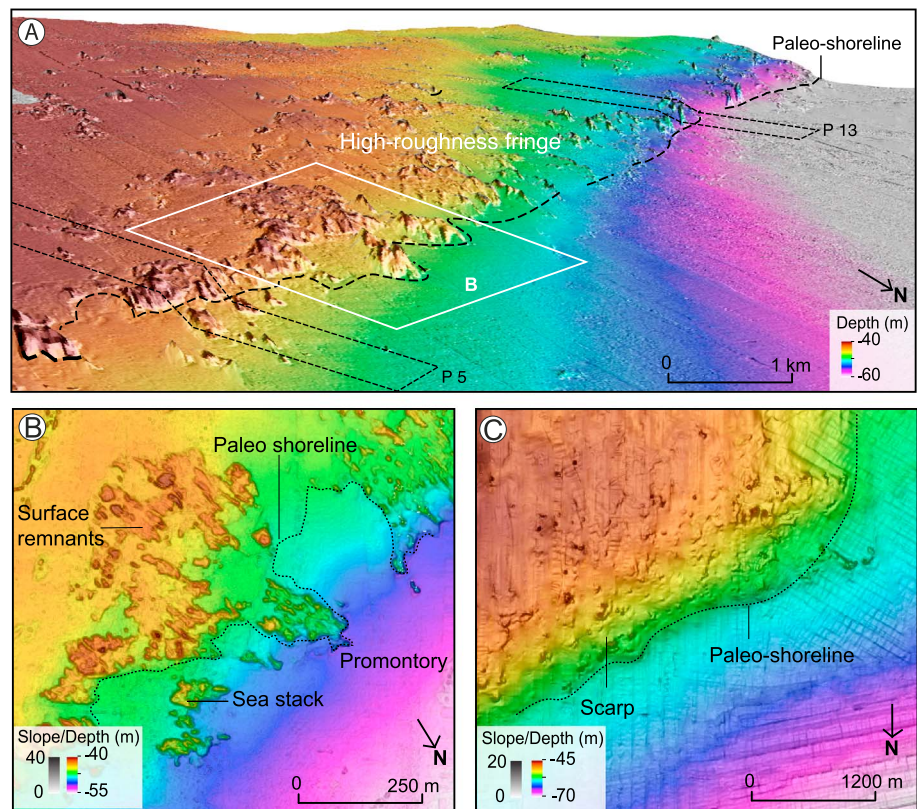
Figure 6. Examples of geomorphic features associated with drowned shorelines along the eastern domain. (a) Perspective view of the arc-shaped scarp denoting the high-roughness fringe that traverses the Arauco Bay (location in Figure 5a). Note the increase in depth of the cliff foot trace to the west. Dashed black rectangles indicate location of swath profiles in Figure 5b. (b) Shaded bathymetry near the mainland off Coronel, where the high-roughness fringe has a rather irregular scarp comprising stacks, promontories, and rocky outcrops. (c) Shaded bathymetry near the center of the bay showing the notorious linear trace of the scarp and sharp character with smooth surface and scattered rocky outcrops. Locations of Figures 6b and 6c are in Figure 5a.

and reaching to the coast off Coronel, and a western domain, centered at the SMI and adjacent areas reaching the edge of the continental slope (Figure 4a). Below we describe the morphology of the Arauco Bay area from east to west, for each of these domains.

The smooth and northward dipping surface of the eastern domain is disrupted by an E-W oriented, ~25 km long arcuate fringe spanning the entire center of the bay between Coronel and SMI (Figures 4a and 5a). In profile view, the fringe represents a submarine scarp that separates the bay seafloor in slopes of 0.25° and 0.5° northward and southward of the scarp, respectively (Figure 5b). The surface morphology of the fringe comprises clustered rough patches mapped by the SCM and defined as shoreline level 1; eastward these patches enclose irregular positive bathymetric features of 8 to 15 m height bounded by small polygonal scarps forming isolated columnar features sculpted into hard substrate and resembling erosional structures developed on scarp faces (Figures 6a and 6b). To the west the scarp trace is less irregular and its surface is smoother comprising scattered rocky outcrops (Figure 6c). The depths of the high-roughness patches from the shoreline level 1 follow a Gaussian distribution with a mean at 48.6 m bsl and standard deviation of 5 m (Figure 5d), suggesting the presence of a distinct, single shoreline level. We analyzed 38 swath profiles along the high-roughness fringe obtaining shoreline angles between 43 and 69 m bsl; the maximum depths of all swath profiles display a convex scarp formed by several peaks that emerge from the smooth surface of AB. Here shoreline angles are generally located in close association with the surface, suggesting the absence of significant diffusion processes. Considering its morphology and continuous trace, the fringe resembles a partly eroded sea cliff bounded by isolated bathymetric peaks resembling sea stacks and promontories (Figure 6b).
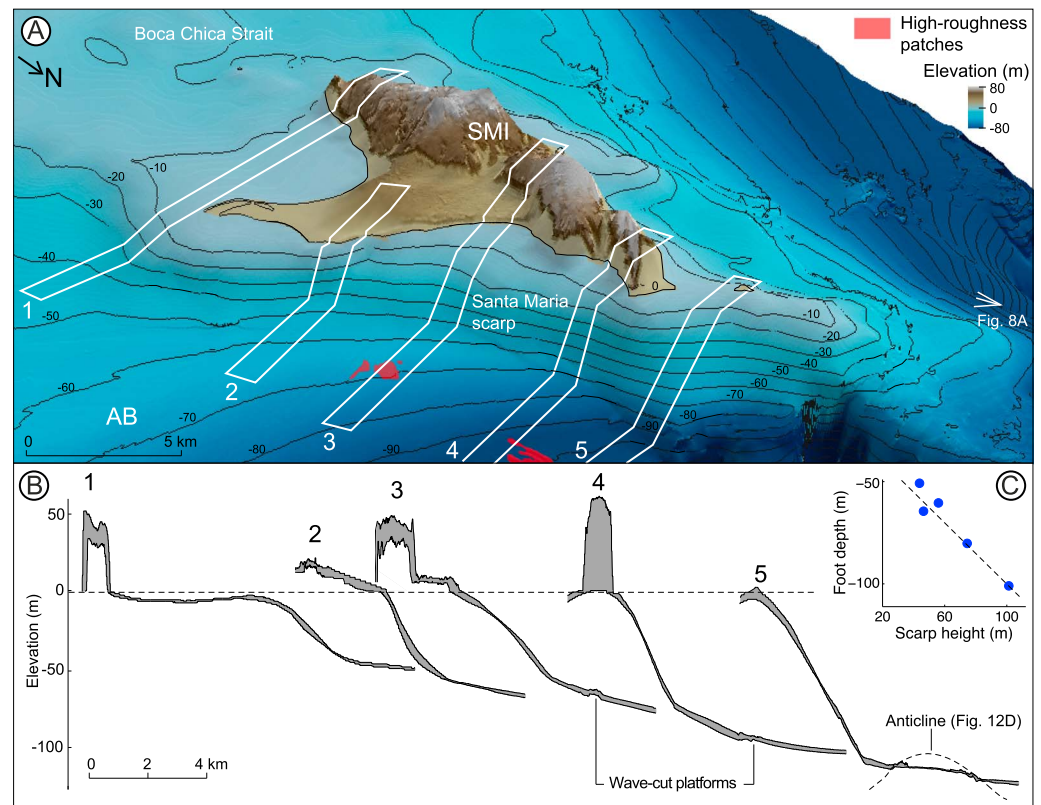
Figure 7. Morphology of the Santa María scarp. (a) Perspective shaded relief view of the scarp to the SW. White rectangles indicate location of swath profiles used to quantify scarp relief. (b) Swath profiles used to analyze the scarp relief. (c) Relation between scarp height and scarp foot depth. Note inverse relation suggesting a tectonic rather than purely erosive origin for the scarp. (See text for details.)

The Santa María scarp is a well-developed feature that separates the deep and smooth bathymetry of the eastern domain from the shallower areas that surrounds SMI in the western domain (Figure 7a). The scarp has a steep slope of ~35° and a linear trace, and its height increases progressively northward reaching 105 m north of SMI (Figure 7b). We studied this scarp using six swath profiles. High-resolution bathymetry covers the scarp foot, where we recognized aligned rocky outcrops between 70 and 130 m bsl, extending ~6 km northward of SMI toward the shelf edge. The top of the scarp is interpreted from bathymetry in existing nautical charts interpolated at a resolution of 20 m (see section 3.1), which allows characterizing the morphology of this feature.

The western domain, west of SMI, consists of a smooth and westward inclined surface (~0.9° slope) disrupted by rocky outcrops at different depths rising from the rather flat adjacent seafloor and partly covered by sediments toward the north (Figure 8a). The rocky outcrops consist of deformed and densely fractured sedimentary units of inferred Tertiary age (based on their similarity with exposed platforms onshore, see supporting information S1 and Figures S5–S7), characterized by high surface roughness confidently classified by the SCM (Figures 8b and 8c). The depth distribution of these outcrops is polymodal characterized by three sharp bands at 119, 90, and 55 m bsl (Figure 9b), representing a staircase sequence of drowned shorelines defined as shoreline levels 4, 3, and 2, respectively (Figure 9a). We analyzed these levels with 22 swath profiles. The uppermost shoreline level 2 comprises high-roughness convex scarps distributed in three main N-S aligned rocky outcrops (Figure 8a); the scarps intersect a smooth platform covered by sediments south of SMI with shoreline angles between 70 and 45 m bsl. The abrasion platform of level 2 is disrupted by corridors and ramps (Figures 9a and 8a), which are typical features of wave-cut platforms developed in high-energy coasts [e.g., *Twidale et al.*, 2005]. The shoreline level 3 comprises the central band of high roughness, a broad platform at ~90 m bsl extending northwest of SMI formed by rocky outcrops partly covered by weak sediments (Figure 9b). Immediately west of SMI, this level is represented by a pronounced cliff sculpted in the bedrock
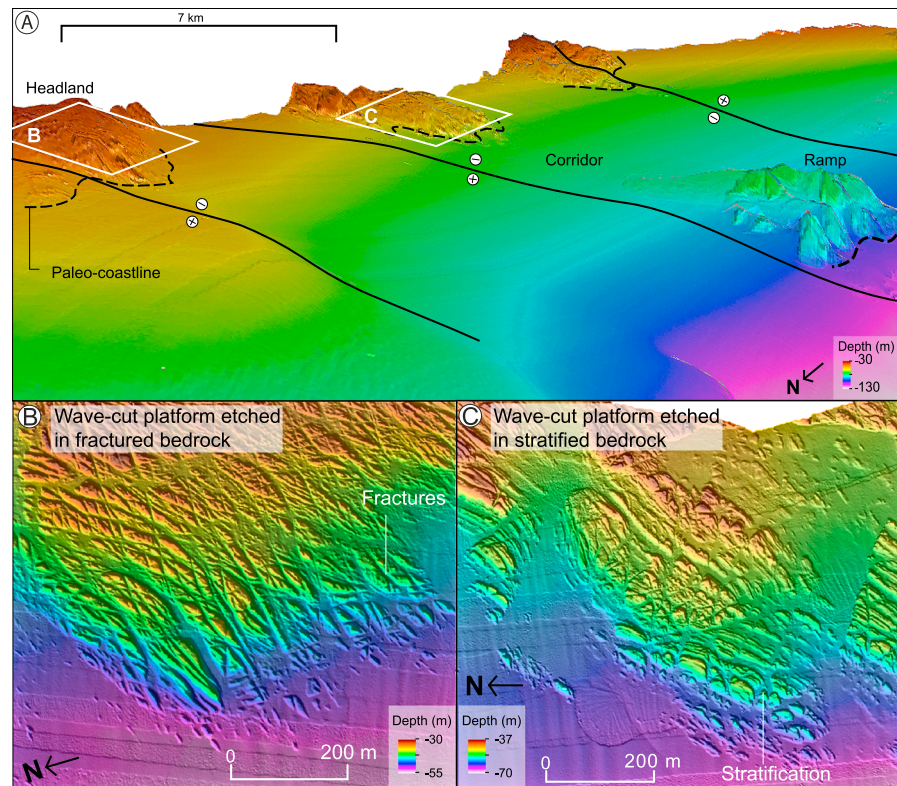
Figure 8. Examples of geomorphic features associated with drowned shorelines along the western domain. (a) Perspective view of the three isolated promontories formed by outcrops of probable Tertiary bedrock depicting remnants of a drowned scarp (location in Figures 7 and 9b). Black lines indicate positions of active faults. (See text for details.) (b and c) Shaded relief maps highlighting the morphology of abrasion platforms and scarps sculpted in deformed and pervasively fractured Tertiary sedimentary rocks. These drowned features resemble exposed platforms along rocky coasts. Locations of Figures 8b and 8c are in Figure 9b.

(Figures 9a and 9b). The lower shoreline level 4 is formed by scattered patches of high roughness reaching ~120 m bsl, bounded by a small scarp and widening north of SMI. Differential erosion processes capable of truncating bedrock stratification are expected to occur only at shallower depths, associated with the effect of wave abrasion that generates wave-cut surfaces. The similarity of these drowned surfaces with active wave-cut platforms nearby (see Figure S7 in the supporting information) suggests that these features were developed a few meters below sea level.

4.2. In Situ Observations at Drowned Shorelines

ROV imaging and sampling were performed along an elongated and pristine-looking sea stack facing the seaward edge of the AB fringe (Figure 10a). The ROV dive started from the top of the structure at 38 m bsl, continuing downward toward its base at 44 m bsl (Figure 10a). The stack top is flat and covered by brown algae and bounded by a 7 m high steep cliff with an ~70° slope (Figures 10a and 10c) sculpted into poorly lithified black sandstone as suggested by fragments collected from the foot of the cliff (Figures 11b and 11c). The foot of the cliff is covered by a chaotic deposit that includes rounded and angular boulders reaching a maximum diameter of 2 m that likely constitute colluvial wedge material (Figures 10b and 10e). At one location the cliff has apparently not yet collapsed and its internal part is exposed revealing a cavity sculpted at its base that we interpret as a wave-cut notch (Figures 10b and 10d); the notch is a sharp, well expressed feature with ~50 cm height and ~70 cm length. The presence of a notch at the base of the cliff suggests that these drowned geomorphic features were formed by wave erosion associated with past sea level positions. The seafloor adjacent to the foot of the cliff below 46 m bsl is covered by sand with decimetric-scale wave ripples, which we sampled for granulometric analysis. The comparison of these sediment samples with those collected at SMI by *Jara-Muñoz and Melnick* [2015] suggests that they were deposited under shallow
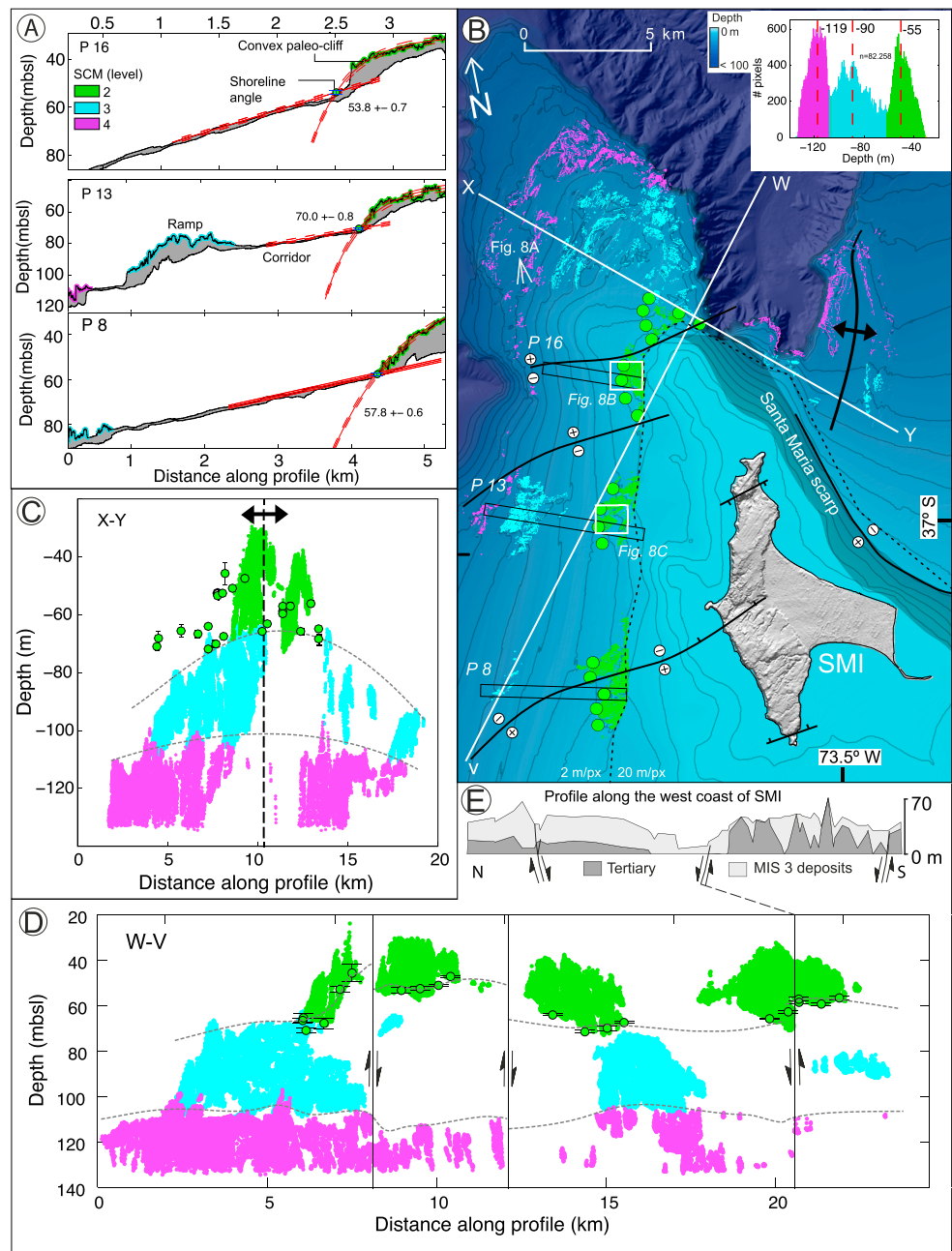
Figure 9. Morphology and structures along the western domain. (a) Swath profiles located along the western coast of Santa María Island. High-roughness areas define three distinct levels between 40 and 120 m bsl. (b) Shaded bathymetry indicating location of drowned shorelines angles (green dots), high-roughness areas (color coded by depth), active structures, and areas of swath profiles in Figure 9a. Inset shows depth distribution of high-roughness areas. Note the three peaks associated with distinct shoreline levels. (c) NW-SE oriented profile showing depth of the high-roughness areas, shoreline angles, and the projected axis of the western anticline. (d) NNE-SSW oriented profile showing distribution of high-roughness areas, shoreline angles, and position of inferred active faults. (e) N-S profile along the western coast of Santa María Island showing simplified geology and active faults [after *Melnick et al.*, 2006].

marine conditions. Cobbles and pebbles collected at 44 m bsl, from the lower parts of the colluvial wedge, show evidences of bioerosion [*Leymerie*, 1841; *Bromley and D'Alessandro*, 1983, 1987; *Bromley*, 1994; *Perry*, 1996] and impact marks [*Whittaker*, 2010] suggesting that these fragments were reworked under high-energy conditions, such as those existing along rocky shorelines frequently impacted by recurrent storms. (Further details on the sedimentology and surface morphology analysis may be found in Figure S8 and
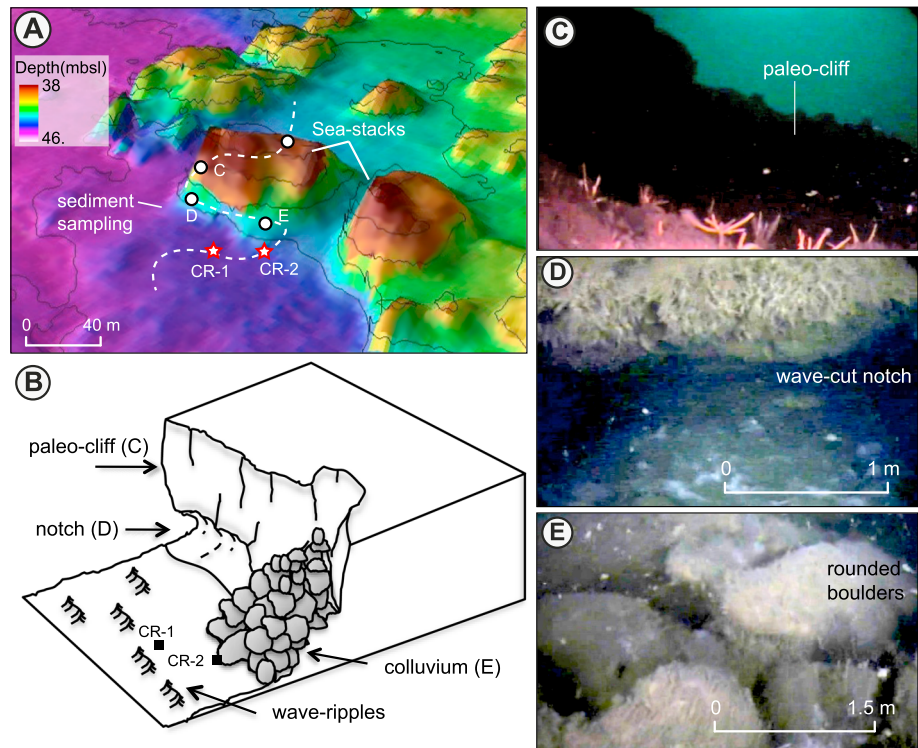
Figure 10. In situ observations of a drowned shoreline features at a dive site in the Eastern Domain. (a) Perspective shaded relief map showing path and location of observations made with a remotely operated vehicle (ROV) and sites CR-1 and CR-2 where professional divers collected samples of sediments and rocks respectively. (b) Schematic representation of the in situ observations made with the ROV. (c) Submarine photo made with the ROV of the drowned paleocliff looking upward from the bottom. (d) Submarine photo of a wave-cut notch at the base of the cliff. (e) Photo of rounded boulders at the base of the cliff, likely deposited by partial localized collapse of the cliff.
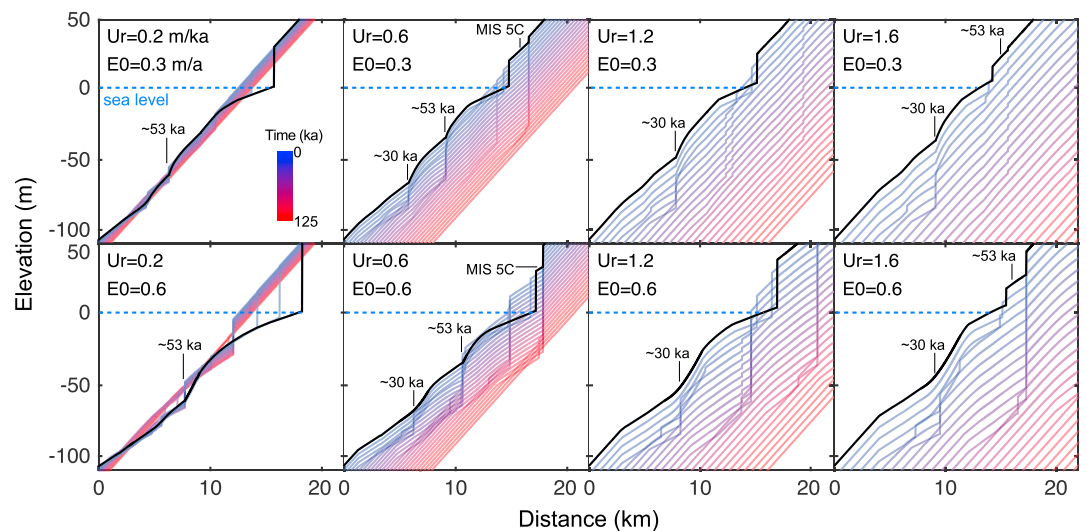
Figure 11. Landscape Evolution Model of wave erosion under oscillatory sea level and steady tectonic uplift. Sensitivity simulations of the model to variable uplift rate (Ur) and initial erosion rate (E0) using a sea level history spanning the past 125 ka compiled from *Siddall et al.* [2003] and *Rohling et al.* [2009]. The ages of distinct levels with higher preservation potential is indicated; colored curves show evolving bathymetry with time. (See text for details.)
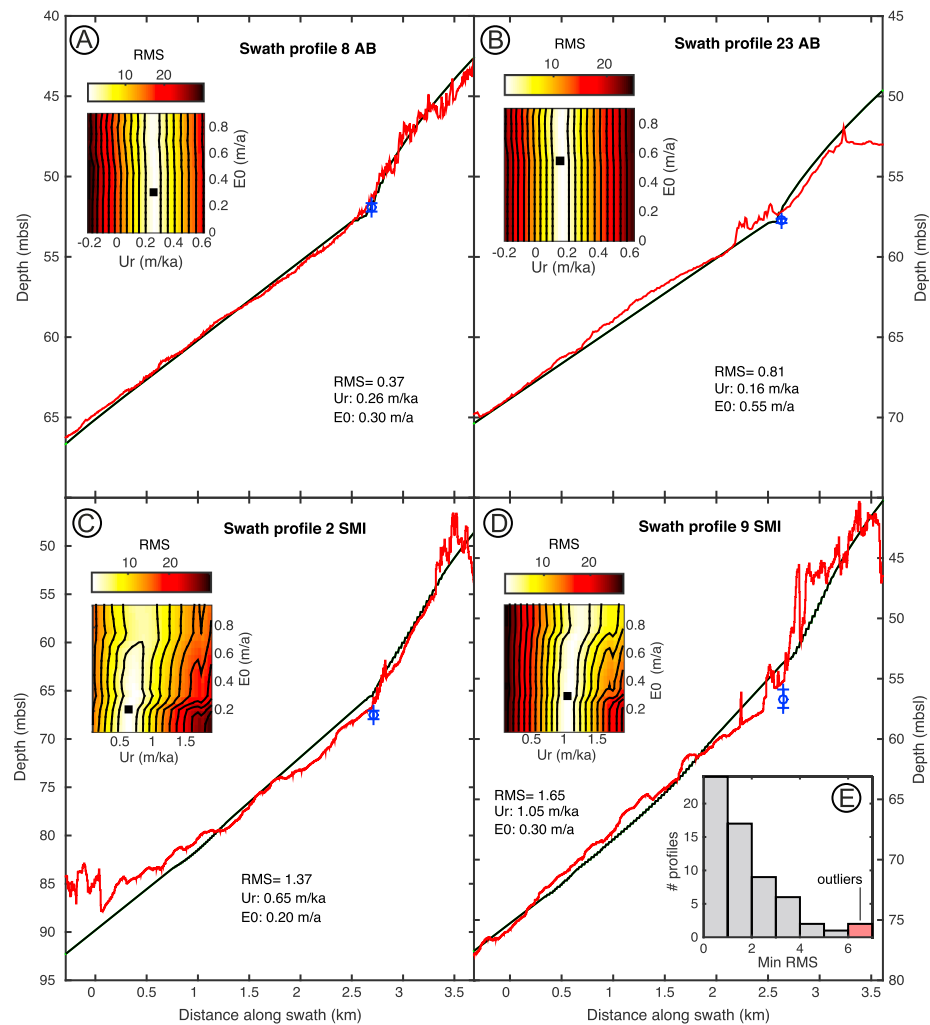
Figure 12. Examples of forward model results showing comparisons between bathymetric swath profiles extracted from the multibeam data and modeled with the Landscape Evolution Model. (a and b) Examples from the eastern domain. (c and d) From the western domain. The insets shows root-mean-square (RMS) space with 2.5 contour lines. Note low dependence on initial erosion (E0) rates and strong dependence on uplift rate (Ur). (e) Histogram of RMS values for all analyzed profiles, red rectangle indicate outliers discarded due to their anomalously high RMS.

supporting information S1, references indicated for bioerosion and impact marks refers to supporting information S1.)

4.3. Distribution of Uplift Rates Inferred From Drowned Shorelines

To estimate uplift rates from drowned shorelines, we compared swath profiles with LEM results. We calibrated the LEM with a sensitivity experiment focused on elucidating the temporal evolution of drowned shoreline levels using the two stacked sea level curves, exploring the contribution of initial erosion rate (E0) and uplift rate (Ur) on surface morphology. We tested several combinations of sea level curves (see supporting information S1 and Figure S3), selecting *Siddall et al.* [2003] and *Rohling et al.* [2009] (Figure 3a) because they have the highest resolution in the time of interest (MIS 5 to 1) and because both curves have been successfully used to estimate uplift rates from MIS 5–3 marine terraces in the region [*Melnick et al.*, 2006; *Jara-Muñoz et al.*, 2015a]. Eight scenarios for the preservation of drowned marine terraces are shown in Figure 11. The initial geometry of the model comprises a 25 km long plane with a slope of 0.5° and a wave base of 12 m, as estimated from satellite altimetry (see supporting information S1 and Figure S1). Our results show that two levels (~53 and ~30 ka) have the highest potential to be preserved, with different expression depending on the initial cliff erosion and uplift rates (Figure 11). A relatively high initial cliff erosion rate
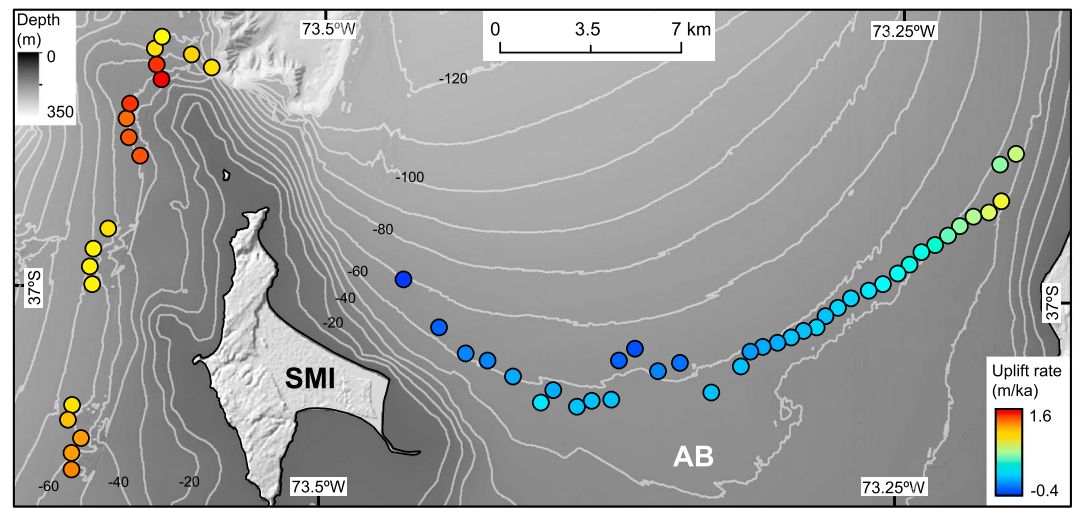
Figure 13. Distribution of uplift rates from Landscape Evolution Model. SMI: Santa María Island, and AB: Arauco Bay.

(0.5 m/a) results in more pronounced, wider terrace levels, whereas lower rates (0.25 m/a) result in smoothed levels located slightly farther inland. We compared the sensitivity to different uplift rates by increasing its value from 0.2 to 1.6 m/ka with 0.4 m/ka increments. At the lowest uplift rates only one sharp slope inflection is formed by reoccupation at 30 ka and 53 ka; as the uplift rate increases, two distinct levels form in normal arrangement with the youngest level located deeper than the oldest one. At the highest uplift rate, the 53 ka level rises above sea level and is preserved as an uplifted marine terrace. This is analogous to the setting at SMI characterized by rapid uplift at ~1.5 m/ka that results in exposure of the ~53 ka wave-cut platform at elevations between 0 and 30 m above sea level.

At SMI, the deposits that cover the ~53 ka platform include a lower marine unit covered by eolian sediments deposited until ~30 ka, suggesting that the coastline was at lower position and distant from the island. Based on these field observations, we correlate the shallower drowned shoreline mapped off the western coast of SMI with the ~30 ka level reproduced by the LEM. On the other hand, the AB is characterized by a single distinct drowned shoreline level, suggesting that it has experienced less uplift than SMI. Therefore, we correlate the drowned AB shoreline angles with the ~53 ka terrace level produced by the LEM simulations with lower uplift rates between ~0 and 0.4 m/ka.

The range in uplift and initial erosion rates obtained from the sensitivity models was used as an input para- meter to estimate the best fitting model that reproduced the minimum depth of each bathymetric swath profile. We compared 130,000 model runs for the total of 61 swath profiles. Figures 12a–12d show examples of model fits and their associated RMS. (Geolocated shoreline angles and modeled profiles can be found in supporting information Data Set S1.) The best fitting models have relatively low RMS values between 0.4 and 6.6 m, suggesting robust results for most, but four profiles from the western domain, which we consid- ered outliers that were discarded due to their anomalously high RMS (Figure 12e). The best fitting initial cliff- erosion rate ranged between 0.1 and 0.6 m/a increasing toward the center of the AB, comprising slightly higher but more scattered values toward the west of SMI. However, there is no evident dependence of E0 to Ur (Figures 12a–12d), which can be attributed to the role of inherited platform topography during sea reoccupation. The resulting uplift rates follow a similar trend as the depth, ranging between −0.04 and 0.4 m/ka across the AB and between 0.5 and 1.6 m/ka around SMI (Figure 13), with associated errors between 0.07 and 0.15 m/ka (Table 1).

4.4. Active Structures in the Arauco Bay Area Mapped From Multibeam Bathymetry

To link the pattern of uplift rates inferred from the drowned shorelines with the mapped faults in the area, we projected the SCM and shoreline-angle depths along different profiles perpendicular to the structures mapped from the high-resolution bathymetry (Figures 5c, 9c, and 9d).

Along the eastern domain both SCM and shoreline-angle depths increase progressively westward from 38 to 69 m bsl delineating an ~22 km wide synform, which is locally disrupted by a secondary fault and a narrow

Table 1. Shoreline Angles and Uplift Rate Estimates[a]

Profile n°	Zone	E	N	Z (m)	Ze (m)	RMS	E0 LEM (m/ka)	Ur LEM (m/ka)	Ur Error (m/ka)	Ur Elastic (m/ka)	Residual (m/ka)
1	ED	660248	5909329	−45.96	0.22	0.36	0.50	0.36	0.11	0.36	0.00
2	ED	659617	5908896	−48.32	0.13	0.46	0.80	0.32	0.10	0.35	0.03
3	ED	659670	5907490	−43.46	1.04	1.02	0.00	0.42	0.12	0.44	0.02
4	ED	659180	5907049	−44.47	1.55	1.22	0.00	0.40	0.12	0.42	0.02
5	ED	658604	5906901	−47.67	1.32	0.85	0.30	0.34	0.11	0.40	0.06
6	ED	658061	5906524	−48.21	0.5	1.07	0.00	0.32	0.11	0.37	0.05
7	ED	657105	5905798	−50.24	1.16	0.73	0.00	0.28	0.10	0.35	0.07
8	ED	656585	5905535	−51.92	0.26	0.37	0.30	0.26	0.10	0.32	0.06
9	ED	656128	5905053	−52.52	0.66	0.97	0.00	0.26	0.10	0.31	0.05
10	ED	655681	5904702	−53.46	0.97	1.02	0.45	0.24	0.10	0.29	0.05
11	ED	655095	5904292	−53.9	1.02	0.85	0.90	0.22	0.10	0.27	0.05
12	ED	654547	5904056	−55.34	0.86	0.75	0.00	0.20	0.09	0.26	0.06
13	ED	653863	5903751	−57.3	0.32	0.53	0.55	0.18	0.09	0.23	0.05
14	ED	657607	5906179	−49.63	0.5	0.98	0.00	0.30	0.10	0.36	0.06
15	ED	653359	5903373	−57.7	0.52	0.89	0.55	0.18	0.09	0.22	0.04
16	ED	652882	5903066	−57.77	0.12	0.30	0.75	0.16	0.09	0.20	0.04
17	ED	652554	5902619	−57.22	0.38	0.51	0.55	0.18	0.09	0.20	0.02
18	ED	652042	5902484	−58.1	0.88	0.63	0.70	0.16	0.09	0.18	0.02
19	ED	651569	5902232	−58.64	0.6	0.48	0.00	0.16	0.09	0.17	0.01
20	ED	651042	5902025	−58.4	0.27	0.63	0.75	0.14	0.09	0.15	0.01
21	ED	650480	5901869	−58.79	0.18	0.43	0.80	0.14	0.09	0.13	−0.01
22	ED	649981	5901704	−59.64	1.24	0.48	0.80	0.12	0.09	0.12	0.00
23	ED	649626	5901121	−57.75	0.12	0.81	0.55	0.16	0.09	0.11	−0.05
24	ED	648485	5900126	−58.12	0.45	1.79	0.75	0.16	0.09	0.10	−0.06
25	ED	647271	5901271	−61.63	0.36	1.67	0.80	0.08	0.09	0.02	−0.06
26	ED	646434	5900937	−60.97	0.17	1.31	0.80	0.10	0.08	0.01	−0.09
27	ED	645531	5901802	−65.76	0.27	0.89	0.80	0.02	0.08	−0.05	−0.07
28	ED	644913	5901354	−62.66	0.11	1.03	0.80	0.04	0.08	−0.02	−0.06
29	ED	644621	5899847	−57.83	0.36	1.99	0.90	0.16	0.09	0.15	−0.01
30	ED	641908	5899731	−57.83	0.66	1.51	0.90	0.20	0.09	0.08	−0.12
31	ED	640832	5900727	−60.06	0.54	1.58	0.90	0.14	0.09	0.01	−0.13
32	ED	639859	5901342	−62.36	0.49	0.80	0.00	0.10	0.08	−0.01	−0.11
33	ED	639002	5901620	−61.02	0.5	0.65	0.00	0.10	0.08	0.04	−0.06
34	ED	637977	5902637	−63.1	0.78	1.15	0.00	0.04	0.08	0.15	0.11
35	ED	636613	5904475	−68.62	0.49	0.73	0.55	−0.04	0.07	0.34	0.38
36	ED	642385	5900221	−58.57	0.28	1.97	0.70	0.14	0.09	0.10	−0.04
37	ED	643874	5899793	−58.93	0.53	1.08	0.00	0.16	0.09	0.18	0.02
38	ED	643307	5899573	−57.26	0.3	0.90	0.80	0.16	0.09	0.18	0.02
1	WD	625216	5906437	−64.17	0.41	2.53	0.05	0.70	0.09	0.68	−0.02
2	WD	624610	5904302	−67.52	0.43	1.37	0.20	0.65	0.08	0.89	0.24
3	WD	624514	5904971	−70.01	1.13	3.48	0.05	0.65	0.09	0.83	0.18
4	WD	624651	5905672	−71.55	0.6	3.50	0.05	0.65	0.09	0.74	0.09
5	WD	623819	5899642	−65.86	0.41	3.01	0.40	0.70	0.09	0.62	−0.08
6	WD	623671	5899071	−62.8	0.59	2.86	0.35	0.80	0.09	1.18	0.38
7	WD	623805	5897800	−59.37	0.67	2.82	0.30	1.00	0.10	0.91	−0.09
8	WD	624173	5898354	−57.25	0.75	5.55	0.45	1.00	0.13	1.02	0.02
9	WD	623812	5897153	−56.68	0.77	1.65	0.30	1.05	0.09	0.83	−0.22
10[b]	WD	618741	5889525	−65.91	0.95	6.40	0.05	0.70	0.10	not used	not used
11[b]	WD	618902	5888777	−55.97	0.92	6.06	0.45	1.00	0.11	not used	not used
12[b]	WD	617662	5886605	−65.11	0.31	6.75	0.15	0.95	0.13	not used	not used
13[b]	WD	617251	5885972	−68.5	1.83	6.61	0.15	0.95	0.12	not used	not used
14	WD	626454	5909244	−47.28	0.48	2.80	0.05	1.40	0.12	1.09	−0.31
15	WD	626032	5909960	−51.18	0.49	4.04	0.05	1.40	0.13	0.92	−0.48
16	WD	625932	5910690	−52.56	0.79	3.72	0.05	1.10	0.12	0.77	−0.33
17	WD	626070	5911264	−53.33	1.43	3.58	0.05	1.55	0.12	0.65	−0.90
18	WD	627278	5912201	−45.72	3.77	2.82	0.15	1.85	0.15	0.96	−0.89
19	WD	627089	5912764	−52.9	1.32	2.92	0.25	1.50	0.11	0.84	−0.66
20	WD	627028	5913376	−67.87	2.3	2.27	0.25	0.70	0.09	0.76	0.06
21	WD	627299	5913835	−70.95	1.23	1.36	0.55	0.50	0.08	0.73	0.23
22	WD	628436	5913149	−65.5	2.07	2.22	0.25	0.75	0.09	0.93	0.18

Table 1. (continued)

Profile n°	Zone	E	N	Z (m)	Ze (m)	RMS	E0 LEM (m/ka)	Ur LEM (m/ka)	Ur Error (m/ka)	Ur Elastic (m/ka)	Residual (m/ka)
23	WD	629216	5912641	−66.62	1.12	2.20	0.95	0.70	0.08	0.76	0.06

[a]WD: western domain, ED: eastern domain, E0 LEM: initial erosion rate, Ur LEM: uplift rate from Landscape Evolution Model (LEM), Ur error: uplift rate error, Ur elastic: uplift rate from preferred elastic model, residual: difference between elastic model and LEM estimates, RMS: root-mean-square error of LEM fit.
[b]Shoreline discarded due to high RMS.

anticline at the eastern and central parts of the bay, respectively (Figure 5c). East of SMI the shoreline angles are locally warped about an ~10 m high and ~5 km wide anticline that slightly offsets the trace of the drowned shoreline. Toward the east along the coast off Coronel the depth of shoreline angles decreases continuously and at the easternmost parts of the bay they are locally offset ~6 m by a NW-SE striking fault (Figures 5a and 5c).

At the western domain we projected shoreline angles and SCM depths along two profiles to assess warping patterns and to estimate vertical displacements by local faults (Figure 9b). The WNW-ENE oriented profile (Figure 9c) reveals an ~15 km wide antiform delineated by all the drowned shoreline levels; the hinge of this anticline is parallel to the NNE-SSW oriented tilt axis of the northern SMI [*Melnick et al.*, 2006]. Along the NNE-SSW oriented section, parallel to the axis of the anticline (Figure 9d), the shoreline angles are displaced by three distinct faults. The southern fault offsets the shoreline angles by ~5 m as well as the SCM depths of the deeper levels. This structure may correspond to the offshore prolongation of a normal fault mapped at the center of SMI [*Melnick et al.*, 2006]. The two additional structures farther north offset the shoreline angles by 9 and 5 m, respectively, and may be similar to those mapped at the northern part of SMI (Figures 9e and 9d).

The area located northeast of SMI including the eastern flank of the Arauco Canyon [*Bernhardt et al.*, 2015] includes different deformed geomorphic features that we link with the surface expression of the main strands of the SMFS (Figure 14a). Several NNE-SSW striking structures deform Tertiary bedrock platforms and the sea-floor. A well-defined graben bounded by subparallel synthetic normal faults is found in the eastern part of the Arauco Canyon (Figure 14b) at ~400 m bsl, with the east bounding fault extending into the Bio-Bio Canyon (BBC) where it controls the position of a prominent knickzone that offsets the canyon thalweg by 40 m, at 750 m bsl [*Bernhardt et al.*, 2015]. This structure is bounded to the south by a group of small curvilinear faults (Figure 14c), which may constitute a transfer zone linking two anticlines that are separated by the Arauco and Bio-Bio canyons (Figures 2 and 14a). These normal faults merge with the flank of an ~2 km wide north plunging anticline located immediately east of SMI. The hinge of the anticline has been eroded by waves exposing its core (Figure 14d). The anticline axis is oriented NNE-SSE and extends southward to the Santa María Scarp. Interestingly, the inverse relation between scarp height and cliff-foot depth along the Santa María Scarp (Figure 7c) is opposite to observations along the AB fringe (Figure 5e). We explain the inverse relation with a continuous growth of the scarp by slip on the underlying SMFS, creating the observed relief.

5. Estimating Fault-Slip Rates Using Dislocation Models

5.1. Structural Model Setups

To link structural observations and estimate the millennial-scale slip rate of the SMFS, we used models based on dislocation theory in an elastic half-space [*Okada*, 1985]. First, we defined two contrasting structural set-ups considering the two hypotheses on the kinematics of the SMFS [*Allmendinger et al.*, 2013; *Melnick et al.*, 2013]: (1) deep-reaching reverse faults (>8 km) and shallow normal faults (<2 km) and (2) shallow and deep-reaching normal faults (Figure 15). The first setup includes deep reverse faults inferred from seismic reflection profiles in the AB and a cluster of seismicity [*Melnick et al.*, 2012b, 2006] as well as normal faults mapped in coal mines at Coronel [*Wenzel et al.*, 1975], exposed at SMI [*Melnick et al.*, 2006, 2012b], and inferred from displaced onshore marine terraces [*Jara-Muñoz et al.*, 2015a]. Although deep-reaching extensional splay faults have not been yet described in the Arauco Bay area, *Aron et al.* [2013] proposed that long-term kinematics in the entire Maule segment is dominated by extensional structures that slip during megathrust
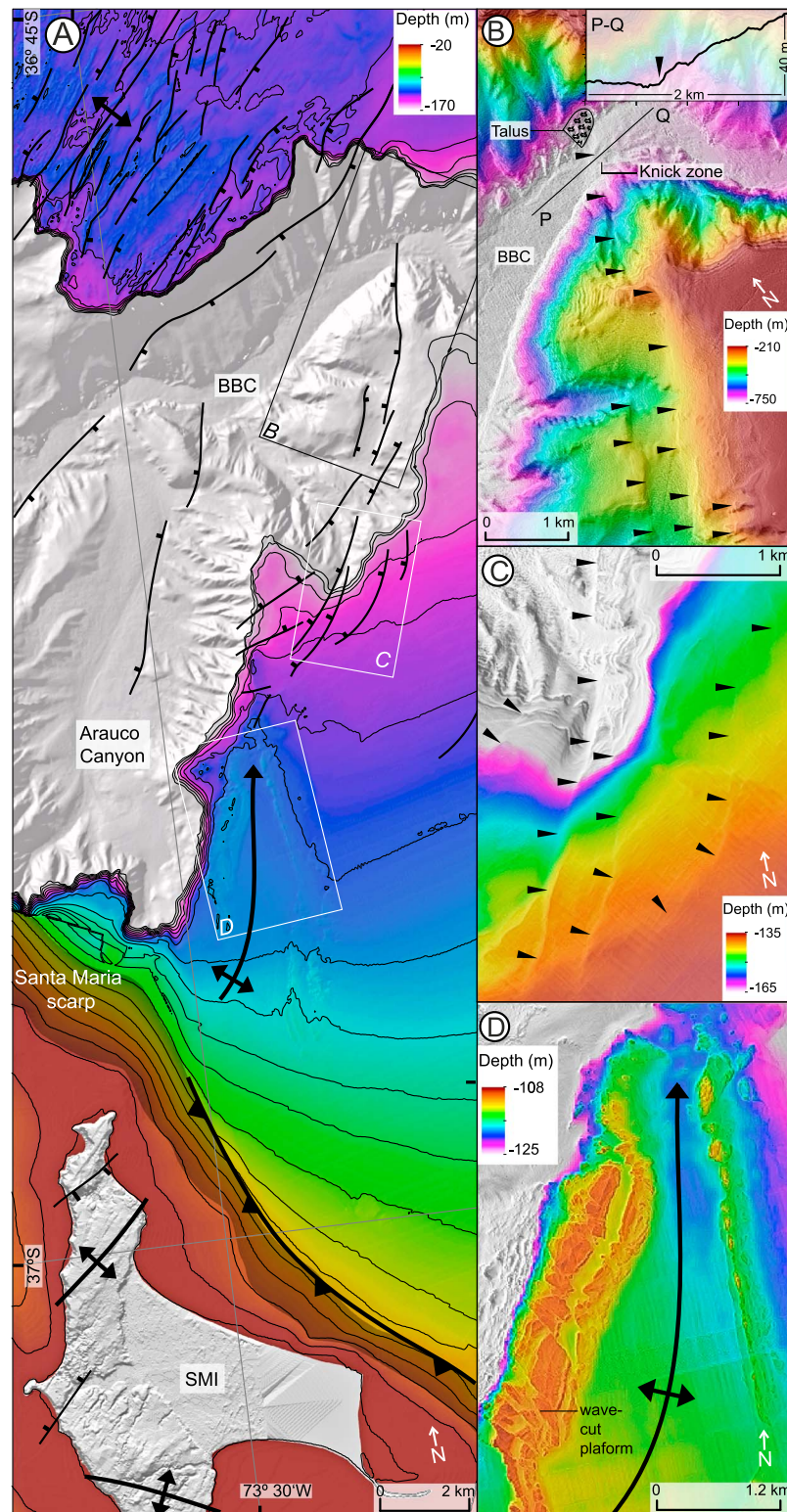
Figure 14. Active structures inferred from multibeam bathymetry between Isla Santa María and the Bio-Bio Canyon (BBC). (a) Shaded relief image showing distribution of structures mapped in this study. (b) Detailed view of graben structures near the BBC. Inset shows talweg profile highlighting the base of a knickzone associated with the intersection of normal faults with the canyon bottom. (c) View of curved normal faults forming a transfer zone between the graben and anticline to the south. (d) View of northward plunging anticline outlined by deformed outcrops of Tertiary rocks. The anticline axis merges southward with the Santa María scarp. Pointers in Figures 14c and 14d indicate the trace of inferred structures.
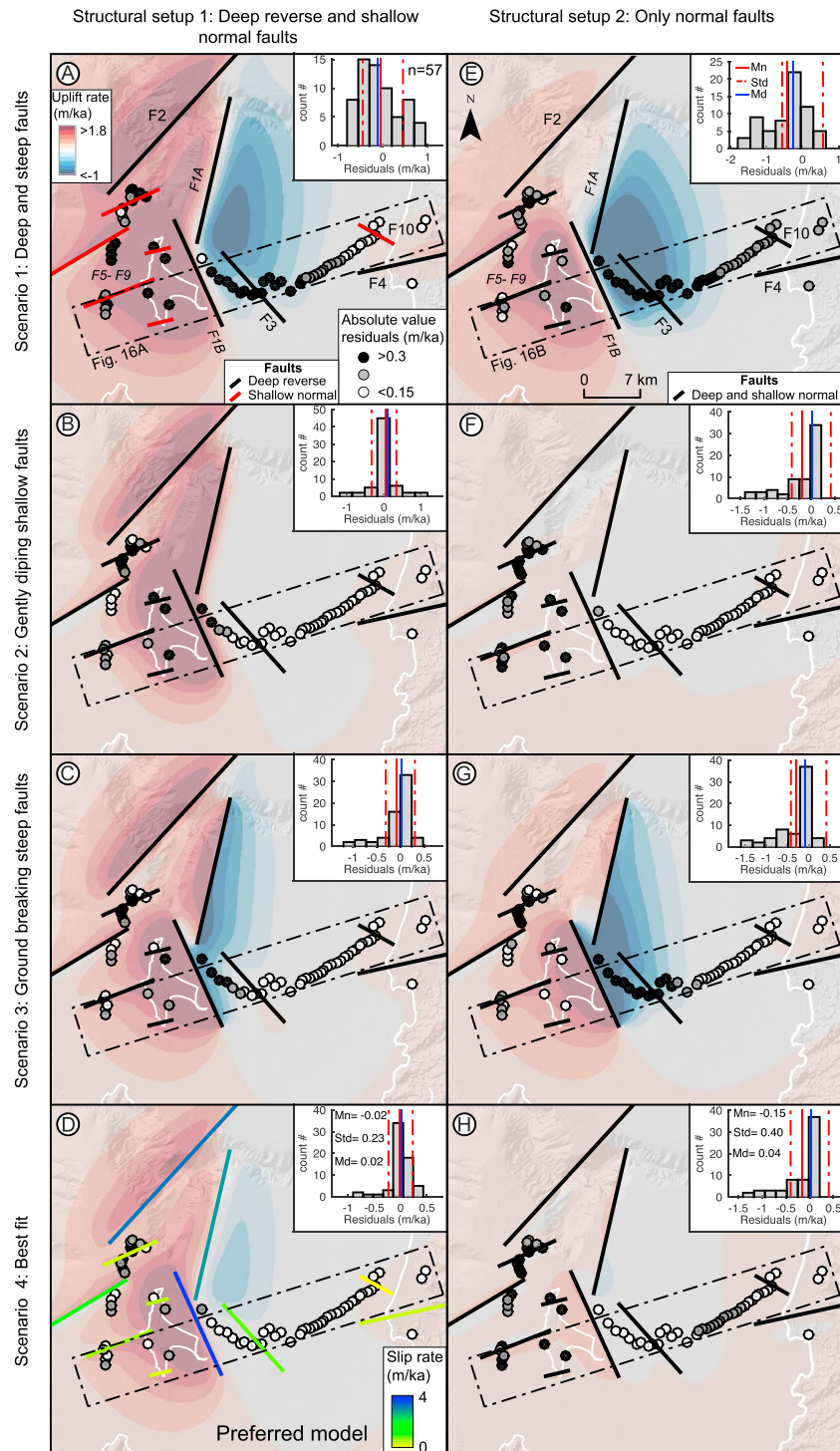
Figure 15. Uplift rates predicted by elastic dislocation modes. The two columns show model setups for deep reverse faults with (a–d) shallow normal faults and (e–h) exclusively normal faults. Rows show different modeling scenarios. Figures 15d and 15h are the best fit models for each setup; Figure 15d is the preferred model. Black thick lines indicate faults included in each model; fault colors in Figure 15d indicate slip rate. Dots denote shoreline angles of drowned shorelines used to calculate residual uplift rates. Black dashed lines indicate the location of swath profiles in Figure 16. Insets show histograms of residual uplift rates. Mn: mean, Std: standard deviation, and Md: median.

Table 2. Fault Parameters of Elastic Models[a]

ID	Scenario 1					Scenario 2					Scenario 3					Scenario 4				
	DDP	UPDP	SLR	DIP	RAKE	DDP	UPDP	SLR	DIP	RAKE	DDP	UPDP	SLR	DIP	RAKE	DDP	UPDP	SLR	DIP	RAKE
								Reverse and Normal Kinematics												
F1A	23	3	4.5	−80	90	12	3	4.5	−55	90	16	0	3.0	−80	90	16	3	3.0	−80	90
F1B	23	3	5.5	−80	90	12	3	5.0	−55	90	16	0	3.7	−75	90	16	3	3.7	−70	90
F2	6	2	3.0	−80	90	6	2	3.0	−80	90	6	2	3.2	−80	90	6	2	3.2	−80	90
F3	5	2	1.2	−40	90	5	2	0.4	−30	90	5	2	1.2	−40	90	5	2	0.8	−40	90
F4	8	3	1.0	−30	90	7	3	0.4	−30	90	8	3	0.4	−30	90	8	3	0.4	−30	90
F5	2	0	1.2	80	−90	2	0	1.2	80	−90	2	0	1.2	80	−90	2	0	1.2	80	−90
F6	2	0	0.7	80	90	2	0	0.7	80	90	2	0	0.7	80	90	2	0	0.7	80	90
F7	2	0	0.4	80	−90	2	0	0.4	80	−90	2	0	0.4	80	−90	2	0	0.4	80	−90
F8	2	0	0.3	80	90	2	0	0.3	80	90	2	0	0.3	80	90	2	0	0.3	80	90
F9	2	0	0.5	80	−90	2	0	0.5	80	−90	2	0	0.5	80	−90	2	0	0.5	80	−90
F10	2	0	0.3	−80	90	2	0	0.1	−80	90	2	0	0.1	−80	90	2	0	0.1	−80	90
								Normal Fault Kinematics												
F1A	23	3	2.0	80	−90	23	0	0.5	55	−90	16	0	2.0	80	−90	12	0	0.8	80	−90
F1B	23	3	6.0	82	−90	23	0	0.5	55	−90	16	0	4.0	85	−90	12	0	1.0	80	−90
F2	6	2	0.7	80	−90	6	2	0.7	80	−90	6	2	0.7	80	−90	6	2	0.7	80	−90
F3	7	2	0.8	78	−90	6	2	0.8	75	−90	5	2	0.8	77	−90	5	2	0.8	83	−90
F4	8	3	0.4	80	−90	8	3	0.4	80	−90	8	3	0.4	80	−90	8	3	0.2	80	−90
F5	2	0	1.2	80	−90	2	0	0.8	80	−90	2	0	1.2	80	−90	2	0	0.8	80	−90
F6	2	0	0.7	80	90	2	0	0.7	80	90	2	0	0.7	80	90	2	0	0.7	80	90
F7	2	0	0.4	80	−90	2	0	0.4	80	−90	2	0	0.4	80	−90	2	0	0.4	80	−90
F8	2	0	0.1	−80	90	2	0	0.1	−80	90	2	0	0.1	−80	90	2	0	0.1	−80	90
F9	2	0	0.5	80	−90	2	0	0.5	80	−90	2	0	0.5	80	−90	2	0	0.5	80	−90
F10	2	0	0.3	80	90	2	0	0.3	80	90	2	0	0.3	80	90	2	0	0.3	80	90

[a]DDP: downdip (km), UPDP: updip (km), SLR: slip rate (m/ka), DIP: (deg), RAKE: (deg), and ID: fault.

earthquakes. Quaternary normal faults have indeed been described along the northern half of the Maule earthquake rupture [*Jara-Muñoz et al.*, 2015a], including the Pichilemu fault that generated *M*6.7 and *M*6.9 earthquakes 11 days after the Maule main shock [*Farías et al.*, 2011; *Ryder et al.*, 2012]. *Allmendinger et al.* [2013] questioned the interpretation of reverse slip along the SMFS during the 2010 event and based on the model of *Aron et al.* [2013] propose normal slip along the SMFS. In an attempt to test the hypothesis of *Aron et al.* [2013] for the long-term control of topography by repeated extensional faulting during megathrust earthquakes, we present a second model setup that includes exclusively normal faults.

5.1.1. Structural Setup 1: Deep Reverse Faults and Shallow Normal Faults

This model included the main NE-SW striking blind reverse fault (F1) associated with the ~70° dipping plane of aligned crustal seismicity (Figures 2 and 15a). F1 is formed by two branches defined as F1A and F1B that strike NNE-SSW and NNW-SSE, respectively (Figure 15a), and for which we increased the dip between 55° and 80° (Table 2). We included two secondary reverse faults located at the rim of the AB following *Melnick et al.* [2012b]: F3, a thrust that branches from F1 dipping between 30° and 40° to the west and linked with F1B at 5 km depth; and F4, a 30° north dipping thrust located near Coronel and extending onshore associated at the surface with F10, a set of normal faults mapped in coal mines [*Wenzel et al.*, 1975] and that locally offset the drowned shorelines (Figure 5c). We included five shallow normal faults, F5 to F9, located west of SMI following observations of shallow faulting in a seismic reflection profile parallel to the island and on outcrops along its western coast [*Melnick et al.*, 2006; *Melnick et al.*, 2012b] (Figure 9e). We assigned dip angles of 80° to these structures and allowed for normal slip to reach the surface. Northwest of SMI a NNE-SSW oriented anticline interpreted from seismic profiles and observed in the high-resolution bathymetry [*Melnick et al.*, 2012b; *Bernhardt et al.*, 2015] has been included as F2 in the model with a dip of 85° and intersecting F1 at 7 km depth following the ramp-flat-ramp upper crustal geometry (Figure 1c).

5.1.2. Structural Setup 2: Normal Faults

We assumed that all structures of the setup 1 have extensional kinematics. We evaluated different scenarios by systematically varying the downdip termination of the main fault to a depth between 12 and 23 km while always allowing slip to reach the surface; this configuration implies that the main splay fault is rooted in deeper parts of the plate interface than in the model setup 1. The secondary faults F2, F3, and F4 were
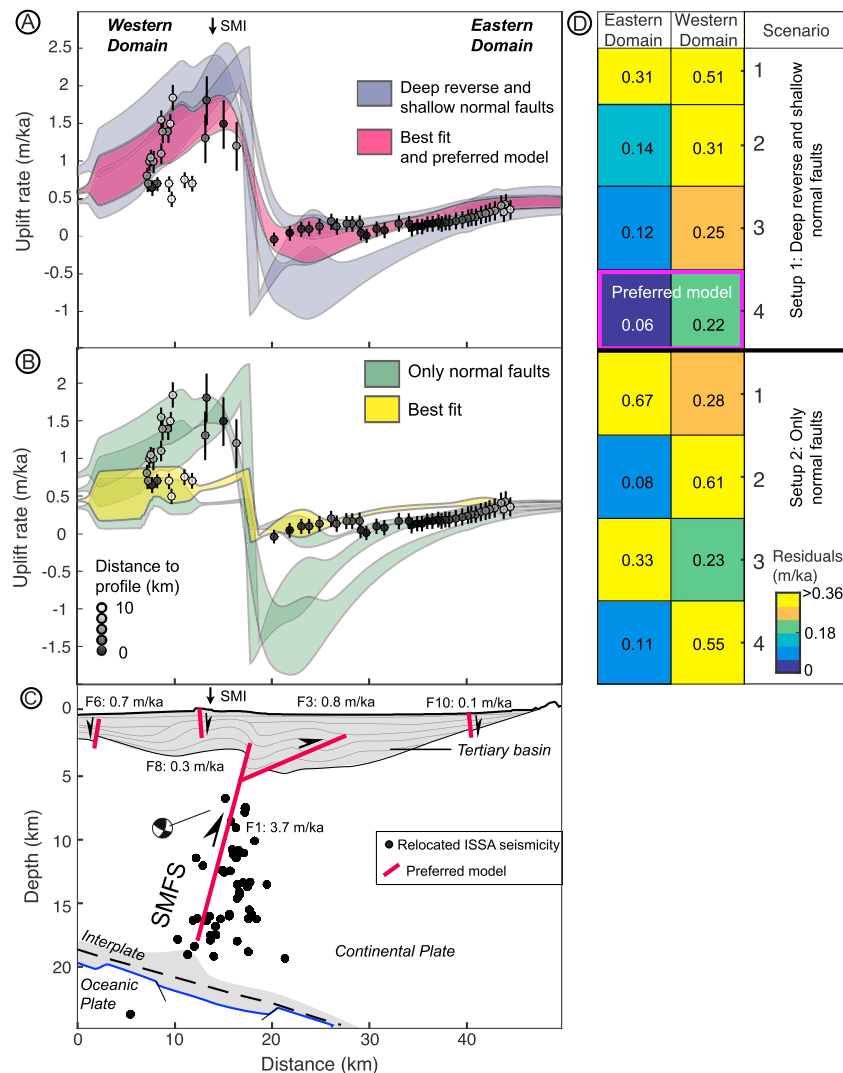
Figure 16. Stacked swath profiles of uplift rates estimated from dislocation models and distribution of residual rates. (a) Reverse fault models. Note that the preferred model successfully reproduces observations in both domains. (b) Normal fault models. Note that the best fit model is unable to reproduce observations at the western domain and the overall warping pattern along the Arauco Bay area. Dots are uplift rates estimated from drowned shorelines with respective error bars. (c) Crustal profile and faults in the preferred model, tertiary basin extent and structure based on seismic line ENAP-017 [*Melnick et al.*, 2006], indicated in Figure 2. The fault slip rate is specified for each fault. Relocated seismicity from the project ISSA [*Bohm et al.*, 2002]. Focal mechanism of crustal *M*4.1 earthquake are from *Bruhn* [2003]. (d) Matrix showing mean residuals for each domain and scenario-setup combination. Note that the preferred model is associated with the lowest residuals at both domains.

modeled with dip angles of 80°, as the shallow normal faults in Model 1 (Table 2), but with downdip depths reaching between 2 and 6 km. The updip extent of slip for faults F3 and F4 was limited to between 2 and 3 km, to better reproduce the deformation patterns in the central part of Arauco Bay.

5.2. Model Results

We determined the model parameters that best reproduce deformation patterns revealed from uplift rates inferred at 64 sites from drowned and emerged shorelines by comparing the distributions of residual rates. Figures 15a–15c, 15e–15g, and 16a and 16b show the deformation patterns for setup 1 and 2 using three end-member scenarios to illustrate the effect of major changes in the input parameters as well as the best fits for both structural setups. The input parameters for these scenarios include the following: strike, length, dip angle, updip and downdip depths, and amount of slip. We fixed the fault strike and length based on our submarine geomorphic and structural mapping (section 4.4). Selected values of updip and downdip are

Table 3. Distribution of Residual Values of Each Elastic Model

	Reverse and Normal Kinematics				Normal Kinematics			
	Scenario 1	Scenario 2	Scenario 3	Scenario 4	Scenario 1	Scenario 2	Scenario 3	Scenario 4
Mean	−0.05	0.05	−0.07	−0.02	−0.42	−0.2	−0.29	−0.15
Median	−0.12	0.1	0.02	0.02	−0.26	0.02	−0.09	0.04
Standard deviation	0.45	0.34	0.31	0.2	0.57	0.41	0.42	0.4

based on published interpretations of seismic reflection profiles (section 2.2) and the relocated crustal seismicity. We compare residuals between model and observations for a range of slip. The four scenarios and two set ups are described below:

The first scenario shows deformation produced by a steep (80° dip) and deep-reaching (23 km depth) F1 blind splay fault with a tip at 3 km. Both model setups fail to reproduce the wavelengths and overall deformation patterns across the Eastern Domain in the scenario 1 (Figures 15a and 15e), with mean residuals of −0.05 and −0.42 m/ka requiring slip rates of 5 and 6 m/ka for setups 1 and 2, respectively (Table 3).

The second scenario includes a gently dipping fault F1 (55° dip) with slip restricted to between 12 km and 3 km depth for setup 1 and to between 23 km and the surface for setup 2. Setups 1 and 2 reproduce well the permanent deformation patterns across the eastern domain requiring slip rates of 5 and 0.5 m/ka, respectively (Figures 15b and 15f) but fail to reproduce the high uplift rate of SMI and the western domain with mean residuals of 0.5 and −0.2 m/ka.

The third scenario includes a steeper (80°) and deeper (16 km) fault F1 with slip reaching the surface. These parameters provide a better fit with the overall deformation patterns and uplift rates in both domains, requiring slip rates of 3.7 and 4.0 m/ka for F1 in setups 1 and 2, respectively, with residuals of 0.07 m/ka. However, uplift rates at the western domain are overestimated by setup 1, and the wavelength of the synform across the eastern domain is underestimated by both setups (Figures 15c and 15g), with residuals of −0.23 m/ka.

The fourth scenario shows the best fit models for setups 1 and 2. For setup 2 it includes a normal fault F1 with downdip depth of 12 km and slip rate of 1 m/ka, which reproduce relatively well the pattern of uplift rates along the easter domain but underestimate them in the western domain (Figures 15h and 16b). The setup 1 best fit model includes a reverse fault F1 with downdip and updip limits at 16 km and 3 km, respectively, with a slip rate of 3.7 ± 0.2 m/ka for the main branch of SMFS (Table 2 and Figure 16a). Our results show that both best fits can approximately reproduce the distribution of permanent deformation for relatively low mean residuals (<0.15 m/ka; Figures 15d and 15h).

6. Discussion

6.1. Millennial-Scale Kinematics and Slip Rate of the SMFS

Two models have been proposed to link deformation during a single earthquake and integrated over several earthquake cycles along the SMFS. *Aron et al.* [2013] proposed that faults favorably oriented to the distribution of coseismic slip might be reactivated as normal faults during megathrust earthquakes and may accumulate permanent upper plate extension. On the other hand, numerical experiments show that the upper plate strain regime leading to reactivation of splay faults during megathrust earthquakes will depend on the position of such faults with respect to the locus of plate boundary slip [e.g., *Melnick et al.*, 2013; *Li et al.*, 2014], controlling both normal and reverse fault kinematics. However, the position of the SMFS with respect to slip during the Maule earthquake is ambiguous; the model of *Tong et al.* [2010] shows an area of high slip (>8 m) east of the SMFS, whereas the model of *Moreno et al.* [2012] suggests higher slip west and below the SMFS (Figure 1b). However, these models are highly smoothed and lack constraints in offshore areas and therefore should be interpreted with caution at the spatial scales of the SMFS. From a regional perspective, the SMFS is located at the edge of the southern patch of slip and may well have been reactivated with reverse slip.

The best fit elastic models (scenario 4 in Figure 15) show that uplift rates and deformation patterns derived from drowned shorelines may be reproduced with relatively low residual rates for both setups (Table 3). However, the choice of a preferred model based exclusively on residuals is not straightforward as
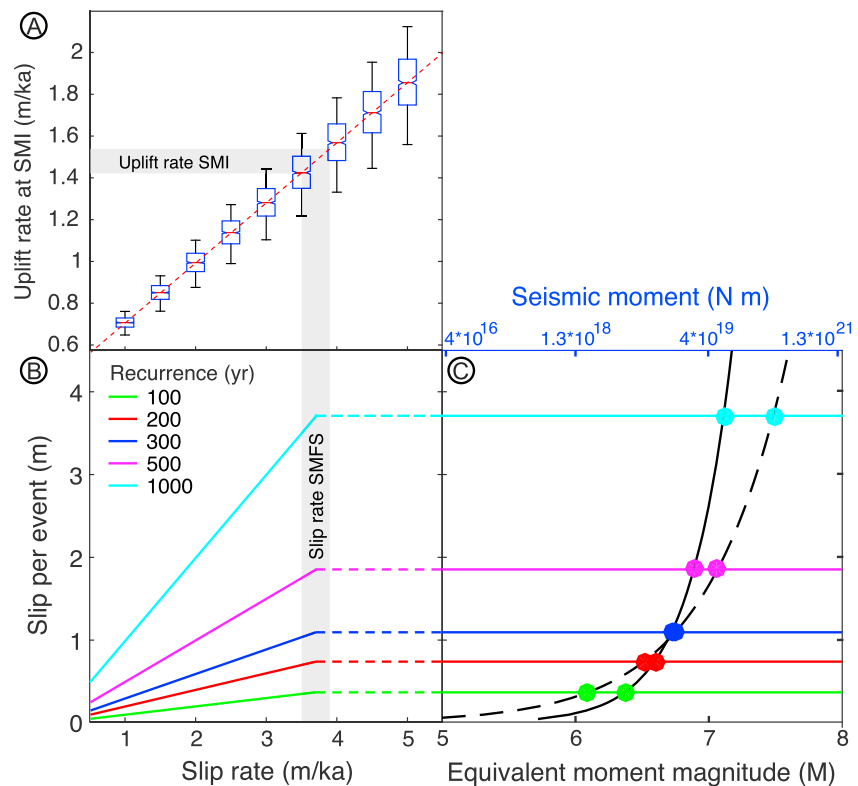
Figure 17. Relation between slip rate of the SMFS, surface uplift, and recurrence time of megathrust earthquakes. (a) Relation between slip rate along the SMFS and uplift rate at SMI estimated from the dislocation models. Note linear relation. Box plots of uplift rate distributions estimated at the area of bathymetry resurveyed by *Wesson et al.* [2015]. (b) Slip along the SMFS per event estimated for different long-term slip rates, assuming that motion along the SMFS occurs exclusively during megathrust earthquakes. (c) Seismic moment of the SMFS slip and the equivalent moment magnitude of an associated earthquake for each recurrence time indicated in Figure 17b. Continuous and dashed lines indicate the empirical relations of *Wells and Coppersmith* [1994] and *Papazachos et al.* [2004], respectively.

observations are not homogeneously distributed. Therefore, we compared mean residuals for each domain, separating the foot and hanging wall blocks of the main SMFS branch (Figure 16d). We selected the best fit of setup 1 as the preferred model as it reproduces the magnitude, amplitude, and wavelength of the deformation patterns in both domains (Figures 15d, 16a, and 16d). Our preferred model suggests slip rates of 3.0 ± 0.2 m/ka and 3.7 ± 0.2 m/ka for F1A and F1B, respectively (the main branches of the SMFS), accurately reproducing the 15 km wide western antiform and 22 km wide eastern synform along the uplift rate profile (Figure 16a). Our preferred model has mean residuals of 0.22 m/ka and 0.06 m/ka for the western and eastern domains, respectively, which are the lowest of all scenario-setup combinations (Figure 16d). Figure 16c synthesizes the reverse kinematics of the preferred model, including structural observations from seismic reflection profiles (see section 2.2), relocated seismicity, and focal mechanisms recorded before the Maule earthquake (see section 2.3). The linear relation between SMFS slip rate and uplift rate estimated at SMI suggests that both rates are linked (Figure 17a) and represent an integrated mean value since ~50 ka, when the drowned shorelines were inundated.

6.2. Splay-Fault Slip During the Megathrust Seismic Cycle

The pattern of permanent deformation across the Arauco Bay can be explained by slip along a system of high-angle, deep reverse faults and secondary, shallow normal faults. However, it is not clear when these structures slip in the seismic cycle context. Upper plate structures of inferred activity during the interseismic phase have been described at New Zealand, northern Chile, and the central part of the Maule earthquake rupture and associated with heterogeneous distribution of megathrust locking, upper plate deformation, and transient slip [*Mountjoy and Barnes*, 2011; *Shirzaei et al.*, 2012; *Jara-Muñoz et al.*, 2015a]. At the Arauco Bay area, the two shallow $M \sim 4$ earthquakes with reverse focal mechanisms registered by the ISSA

network in the year 2000 (Figure 2) might be associated with slip along the SMFS during the interseismic phase. However, no seismicity was recorded in this area by the TIPTEQ network that was installed during an entire year in 2004–2005 [*Haberland et al.*, 2009]. A M_w 6.3 event with reverse focal mechanism and located at 11 km depth below AB occurred in 1990 (National Earthquake Information Center (NEIC) Catalogue, Figure 2), which may be also associated with the SMFS. These isolated events highlight the transient nature of interseismic crustal seismicity in this area, which might suggest that permanent deformation is accrued during transient pulses of splay-fault slip driven by upper plate contraction due to interseismic locking of the megathrust. *Moreno et al.* [2008] explored this hypothesis using a limited number of campaign GPS measurements to determine ~7 mm/yr of shortening across the SMFS during the interseismic period. However, this rate depends on the fault geometry and the distribution of interplate locking, and the authors assumed unconstrained structures and uniform locking, which might introduce a significant bias. These isolated lines of evidence might suggest that interseismic slip along the SMFS is not robust to explain the accumulated pattern of permanent deformation along SMFS.

Studies of splay faults in Japan, New Zealand, Sumatra, Ecuador, Perú, and Cascadia [*Clarke and Carver*, 1992; *Barnes et al.*, 2002; *Park et al.*, 2002; *Audin et al.*, 2008; *Collot et al.*, 2008; *Hoechner et al.*, 2008; *Sakaguchi et al.*, 2011; *Singh et al.*, 2011] have proposed that slip along such structures may often accompany megathrust earthquakes. However, direct observations have been made only during the 1964 Alaska and 2010 Maule earthquakes [*Plafker*, 1967; *Melnick et al.*, 2012b]. At SMI, similarities in tilt patterns of emerged Holocene beach ridges [*Bookhagen et al.*, 2006] and deformation observed by satellite interferometry during the 2010 Maule earthquake [*Melnick et al.*, 2012b] suggest that permanent uplift and tilt of the island, and hence slip along the SMFS, accumulates during great megathrust earthquakes.

Paleoseismic data from Japan [e.g., *Toda and Tsutsumi*, 2013], and the overall lack of direct observations of splay faulting during megathrust earthquakes, suggest that these upper plate structures slip every several great megathrust events. If we assume that slip along the SMFS occurs exclusively during each single megathrust earthquake with a recurrence time of 150 to 200 years, as determined from historic and paleoseismic data [e.g., *Lomnitz*, 2004; *Bookhagen et al.*, 2006], the fault would need to slip between 0.4 and 0.7 m per event to account for the 3.7 m/ka millennial slip rate (Figure 17b). This amount of slip would release a seismic moment of between 1.8×10^{18} and 5×10^{18} Nm, equivalent to a M_w 6.1 to 6.4 earthquake (Figure 17c). However, if the SMFS slips only every ~1000 years, representing five to six megathrust earthquake cycles, then a slip of ~3.7 m per event would be required to account for the long-term rate (Figure 17b), which would be equivalent to a seismic moment release of between 5.6×10^{19} Nm and 2.2×10^{20} Nm, or a M_w 7.1 to M_w 7.5 earthquake (Figure 17c). Such an event could constitute a secondary source for a tsunami.

A comparison of our results from the SMFS with those from other splay faults may provide further insight into the processes and recurrence time of SMFS. The Yunodake fault ruptured after the Tohoku earthquake and has a recurrence time of ~12–17 ka [*Toda and Tsutsumi*, 2013], implying that it ruptures every several great earthquakes. However, this fault has a normal kinematics, is located farther inland and not rooted in the plate interface, and might thus have a different behavior. The Lachlan fault in New Zealand shares similar kinematics and slip rates with the SMFS (3.0–6.5 m/ka) and has the potential to produce M_w 7.6 to 8 earthquakes with a recurrence time of ~1 ka [*Barnes et al.*, 2002]. Several splay faults have been mapped in the Prince Williams Sound, Alaska, at ~150 km from the trench slip with slip rates of ~3.7 m/ka and the potential to produce M_w 7–8 earthquakes [*Finn et al.*, 2015]. In turn, splay faults located at ~50 km from the trench slip at up to ~9 m/ka [*Liberty et al.*, 2013] and earthquakes on these structures have an estimated recurrence time of ~790 years, expecting to be reactivated during most megathrust earthquakes. Splay-fault ruptures in Alaska have been associated with tsunamis [*Liberty et al.*, 2013; *Finn et al.*, 2015; *von Huene et al.*, 2016]. *Liberty et al.* [2013] showed that many of these splay faults slipped together during the 1964 Alaska earthquake forming metric scarps on the seafloor and acting as a secondary source for the tsunami. The similarities between these structures and the SMFS may suggest a similar tsunamigenic behavior, which needs to be explored by a dedicated tsunami modeling study.

7. Conclusions

We studied the pattern of permanent deformation of a splay fault in a fore-arc setting—the Santa María Fault System. Our study highlights the application of quantitative geomorphology with high-resolution

bathymetry to estimate offshore deformation rates. We provide evidence of active structures in the Arauco Bay area that may help improving current models of tsunami inundation and our understanding of fore-arc deformation processes in offshore areas. Our findings and interpretations can be synthetized in three points:

1. Uplift rates between −0.04 and 0.4 m/ka at the eastern domain and between 0.3 and 1.3 at the western domain were estimated by fitting LEM-derived bathymetry to the minimum depth of swath profiles extracted from the multibeam data.
2. We reproduced the spatial distribution of these uplift rates using elastic dislocation models in which the Santa María Fault System is an integral part of a deep-reaching and blind high-angle reverse fault rooted in the plate interface, with a slip rate between 3 and 3.7 m/ka. Normal faults observed in the region appear to be secondary structures that only affect the shallow levels of the crust.
3. Assuming that the millennial-scale slip rate of the SMFS is exclusively accounted for by triggered motion during each single great megathrust earthquakes allows estimating a slip per event of 0.3–0.7 m for the historical recurrence period of ~150–200 years, which would be equivalent to a M_w ~ 6.4 earthquake. In turn, if motion along the SMFS is triggered by earthquakes with a recurrence of ~1000 years, then a slip per event of ~3.7 m would be required to account for the long-term rate, equivalent to a M_w ~ 7.5 earthquake. Such an event could be a secondary source for a local tsunami.

References

Allmendinger, R. W., G. González, J. Cembrano, F. Aron, and G. Yañez (2013), Splay fault slip during the M_w 8.8 2010 Maule Chile earthquake: COMMENT, *Geology*, *41*(12), e309–e309.

Anderson, R., A. Densmore, and M. Ellis (1999), The generation and degradation of marine terraces, *Basin Res.*, *11*(1), 7–19.

Anderson, R. S., and K. M. Menking (1994), The Quaternary marine terraces of Santa Cruz, California: Evidence for coseismic uplift on two faults, *Geol. Soc. Am. Bull.*, *106*(5), 649–664.

Angermann, D., J. Klotz, and C. Reigber (1999), Space-geodetic estimation of the nazca-south America euler vector, *Earth Planet. Sci. Lett.*, *171*(3), 329–334.

Aron, F., R. W. Allmendinger, J. Cembrano, G. González, and G. Yañez (2013), Permanent fore-arc extension and seismic segmentation: Insights from the 2010 Maule earthquake, Chile, *J. Geophys. Res. Solid Earth*, *118*, 724–739.

Arz, H. W., F. Lamy, A. Ganopolski, N. Nowaczyk, and J. Patzold (2007), Dominant Northern Hemisphere climate control over millennial-scale glacial sea-level variability, *Quat. Sci. Rev.*, *26*(3), 312–321.

Audin, L., P. Lacan, H. Tavera, and F. Bondoux (2008), Upper plate deformation and seismic barrier in front of Nazca subduction zone: The Chololo fault system and active tectonics along the coastal cordillera, southern Peru, *Tectonophysics*, *459*(1), 174–185.

Barnes, P. M., A. Nicol, and T. Harrison (2002), Late Cenozoic evolution and earthquake potential of an active listric thrust complex above the Hikurangi subduction zone, New Zealand, *Geol. Soc. Am. Bull.*, *114*(11), 1379–1405.

Beaman, R. J., P. E. O'Brien, A. L. Post, and L. De Santis (2011), A new high-resolution bathymetry model for the Terre Adélie and George V continental margin, East Antarctica, *Antarct. Sci.*, *23*(01), 95–103.

Bernhardt, A., D. Melnick, J. Jara-Muñoz, B. Argandoña, J. González, and M. R. Strecker (2015), Controls on submarine canyon activity during sea-level highstands: The Biobio canyon system offshore Chile, *Geosphere*, *11*(4), 1226–1255.

Berryman, K. (1993), Age, height, and deformation of Holocene marine terraces at Mahia Peninsula, Hikurangi subduction margin, New Zealand, *Tectonics*, *12*(6), 1347–1364.

Bloom, A., W. Broecker, J. Chappell, R. Matthews, and K. Mesolella (1974), Quaternary sea level fluctuations on a tectonic coast: New [230]Th[234]U dates from the Huon Peninsula, New Guinea, *Quatern. Res.*, *4*(2), 185–205.

Bohm, M., S. Lüth, H. Echtler, G. n. Asch, K. Bataille, C. Bruhn, A. Rietbrock, and P. Wigger (2002), The southern Andes between 36° and 40°S latitude: Seismicity and average seismic velocities, *Tectonophysics*, *356*(4), 275–289.

Bookhagen, B., H. P. Echtler, D. Melnick, M. R. Strecker, and J. Q. G. Spencer (2006), Using uplifted Holocene beach berms for paleoseismic analysis on the Santa María Island, south-central Chile, *Geophys. Res. Lett.*, *33*, L15302, doi:10.1029/2006GL026734.

Bourke, M. C., J. A. Brearley, R. Haas, and H. A. Viles (2007), *A Photographic Atlas of Rock Breakdown Features in Geomorphic Environments*, 88 pp., Planet. Sci. Inst., Tucson, Ariz.

Bowles, C. J., and E. Cowgill (2012), Discovering marine terraces using airborne LiDAR along the Mendocino-Sonoma coast, northern California, *Geosphere*, *8*(2), 386–402.

Bradley, W. C. (1958), Submarine abrasion and wave-cut platforms, *Geol. Soc. Am. Bull.*, *69*(8), 967–974.

Briggs, R. W., S. E. Engelhart, A. R. Nelson, T. Dura, A. C. Kemp, P. J. Haeussler, D. R. Corbett, S. J. Angster, and L.-A. Bradley (2014), Uplift and subsidence reveal a nonpersistent megathrust rupture boundary (Sitkinak Island, Alaska), *Geophys. Res. Lett.*, *41*, 2289–2296, doi:10.1002/2014GL059380.

Briggs, R. W., K. Sieh, W. H. Amidon, J. Galetzka, D. Prayudi, I. Suprihanto, N. Sastra, B. Suwargadi, D. Natawidjaja, and T. G. Farr (2008), Persistent elastic behavior above a megathrust rupture patch: Nias island, West Sumatra, *J. Geophys. Res.*, *113*, B12406, doi:10.1029/2008JB005684.

Bromley, G. R. (1994), *The Palaeoecology of Bioerosion, Palaeobiology of Trace Fossils*, pp. 134–154, Wiley, London.

Bromley, R. G., and A. D'Alessandro (1983), Bioerosion in the Pleistocene of southern Italy: Ichnogenera Caulostrepsis and Maeandropolydora, *Riv. Ital. Paleontol. Stratigr.*, *89*, 283–309.

Bromley, R. G., and A. D'Alessandro (1987), Bioerosion of the Plio-Pleistocene transgression of southern Italy, *Riv. Ital. Paleontol. Stratigr.*, *93*, 379–442.

Bruhn, C. (2003), Momententensoren hochfrequenter Ereignisse in Südchile: University of Potsdam.

Cabioch, G., and L. K. Ayliffe (2001), Raised coral terraces at Malakula, Vanuatu, Southwest Pacific, indicate high sea level during marine isotope stage 3, *Quatern. Res.*, *56*(3), 357–365.

Chapman, J. B., J. Elliott, D. I. Doser, and T. L. Pavlis (2014), Slip on the Suckling Hills splay fault during the 1964 Alaska earthquake, *Tectonophysics*, *637*, 191–197.

Chappell, J. (1974), Geology of coral terraces, Huon Peninsula, New Guinea: A study of Quaternary tectonic movements and sea-level changes, *Geol. Soc. Am. Bull.*, *85*(4), 553–570.

Chaytor, J. D., C. Goldfinger, M. A. Meiner, G. J. Huftile, C. G. Romsos, and M. R. Legg (2008), Measuring vertical tectonic motion at the intersection of the Santa Cruz, Catalina Ridge and Northern Channel Islands platform, California Continental Borderland, using submerged paleoshorelines, *Geol. Soc. Am. Bull.*, *120*, 7–8, 1053–1071.

Chlieh, M., J.-P. Avouac, V. Hjorleifsdottir, T.-R. A. Song, C. Ji, K. Sieh, A. Sladen, H. Hebert, L. Prawirodirdjo, and Y. Bock (2007), Coseismic slip and afterslip of the great M_w 9.15 Sumatra-Andaman earthquake of 2004, *Bull. Seismol. Soc. Am.*, *97*(1A), S152–S173.

Cisternas, M., D. Melnick, L. Ely, R. Wesson, and R. Norambuena (2010), Similarities between the great Chilean earthquakes of 1835 and 2010, in Proceedings Chapman Conference on Giant Earthquakes and their Tsunamis, AGU2010, Volume 19.

Clarke, S. H., Jr., and G. A. Carver (1992), Late Holocene tectonics and paleoseismicity, southern Cascadia subduction zone, *Science*, *255*(5041), 188.

Collot, J.-Y., W. Agudelo, A. Ribodetti, and B. Marcaillou (2008), Origin of a crustal splay fault and its relation to the seismogenic zone and underplating at the erosional north Ecuador-south Colombia oceanic margin, *J. Geophys. Res.*, *113*, B12102, doi:10.1029/2008JB005691.

Dahlen, F., J. Suppe, and D. Davis (1984), Mechanics of fold-and-thrust belts and accretionary wedges: Cohesive Coulomb theory, *J. Geophys. Res.*, *89*(B12), 10,087–10,101.

Darwin, C. (1851), Geological observations of South America, London, smith, elder, Geological observations on coral reefs, Volcanic Islands and on South America-Being the Voyage of the Beagle, Under the Command of Captain Fitzroy, R.N., During the years 1832 to 1836, 279 p.

Dickinson, W. R. (2013), Control of paleoshorelines by trench forebulge uplift, loyalty Islands, *Quatern. Res.*, *80*(1), 125–137.

Emery, K. (1958), Shallow submerged marine terraces of Southern California, *Geol. Soc. Am. Bull.*, *69*(1), 39–60.

Farías, M., D. Comte, S. Roecker, D. Carrizo, and M. Pardo (2011), Crustal extensional faulting triggered by the 2010 Chilean earthquake: The Pichilemu seismic sequence, *Tectonics*, *30*, TC6010, doi:10.1029/2011TC002888.

Finn, S. P., L. M. Liberty, P. J. Haeussler, and T. L. Pratt (2015), Landslides and megathrust splay faults captured by the late Holocene sediment record of eastern Prince William Sound, Alaska, *Bull. Seismol. Soc. Am.*, *105*, 2343–2353.

FitzRoy, R., P. P. King, and C. Darwin (1839), Narrative of the surveying voyages of His Majesty's Ships Adventure and Beagle between the years 1826 and 1836: Describing their examination of the southern shores of South America, and the Beagle's circumnavigation of the globe, H. Colburn.

Frankel, K. L., and J. F. Dolan (2007), Characterizing arid region alluvial fan surface roughness with airborne laser swath mapping digital topographic data, *J. Geophys. Res.*, *112*, F02025, doi:10.1029/2006JF000644.

Fukao, Y. (1979), Tsunami earthquakes and subduction processes near deep-sea trenches, *J. Geophys. Res.*, *84*(B5), 2303–2314.

Gallen, S., K. Wegmann, D. Bohnenstiehl, F. Pazzaglia, M. Brandon, and C. Fassoulas (2014), Active simultaneous uplift and margin-normal extension in a forearc high, Crete, Greece, *Earth Planet. Sci. Lett.*, *398*, 11–24.

González, G., P. Salazar, J. P. Loveless, R. W. Allmendinger, F. Aron, and M. Shrivastava (2015), Upper plate reverse fault reactivation and the unclamping of the megathrust during the 2014 northern Chile earthquake sequence, *Geology*, *43*(8), 671–674.

González-Acuña, J., and E. Arroyo-Suarez (2013), Comparative methodologies for sounding reduction applied to a bathymetric survey referred to the WGS-84 ellipsoid, Executed in Concepcion Bay and Gulf of Arauco, VIII Region, Chile., U.S. Hydro 2013, Volume 1: New Orleans, La.

Haberland, C., A. Rietbrock, D. Lange, K. Bataille, and T. Dahm (2009), Structure of the seismogenic zone of the southcentral Chilean margin revealed by local earthquake traveltime tomography, *J. Geophys. Res.*, *114*, B01317, doi:10.1029/2008JB005802.

Hanks, T. C., R. C. Bucknam, K. R. Lajoie, and R. E. Wallace (1984), Modification of wave-cut and faulting-controlled landforms, *J. Geophys. Res.*, *89*(B7), 5771–5790.

Hicks, S. P., and A. Rietbrock (2015), Seismic slip on an upper-plate normal fault during a large subduction megathrust rupture, *Nat. Geosci.*, *8*(12), 955–960.

Hicks, S. P., A. Rietbrock, I. M. Ryder, C.-S. Lee, and M. Miller (2014), Anatomy of a megathrust: The 2010 M8. 8 Maule, Chile earthquake rupture zone imaged using seismic tomography, *Earth Planet. Sci. Lett.*, *405*, 142–155.

Hoechner, A., A. Y. Babeyko, and S. V. Sobolev (2008), Enhanced GPS inversion technique applied to the 2004 Sumatra earthquake and tsunami, *Geophys. Res. Lett.*, *35*, L08310, doi:10.1029/2007GL033133.

Hyndman, R., and K. Wang (1995), The rupture zone of Cascadia great earthquakes from current deformation and the thermal regime, *J. Geophys. Res.*, *100*(B11), 22133–22154.

Imbrie, J., J. Hays, D. Martinson, A. McIntyre, A. C. Mix, J. J. Morley, N. G. Pisias, W. L. Prell, and N. J. Shackleton (1984), *The Orbital Theory of Pleistocene Climate: Support From a Revised Chronology of the Marine d18O Record: Milankovitch and Climate*, pp. 269–305, D. Reidel, Norwell, Mass.

Isla, F. I., J. Q. Flory, C. Martínez, A. Fernández, and E. Jaque (2012), The evolution of the Bio Bio Delta and the coastal plains of the Arauco Gulf, Bio Bio region: The Holocene sea-level curve of Chile, *J. Coast. Res.*, *28*, 102–111.

Jara-Muñoz, J., and D. Melnick (2015), Unraveling sea-level variations and tectonic uplift in wave-built marine terraces, Santa María Island, Chile, *Quatern. Res.*, *83*(1), 216–228.

Jara-Muñoz, J., D. Melnick, D. Brill, and M. R. Strecker (2015a), Segmentation of the 2010 Maule Chile earthquake rupture from a joint analysis of uplifted marine terraces and seismic-cycle deformation patterns, *Quat. Sci. Rev.*, *113*, 171–192.

Jara-Muñoz, J., D. Melnick, and M. R. Strecker (2015b), TerraceM: A MATLAB(R) tool to analyze marine and lacustrine terraces using high-resolution topography, *Geosphere*, *12*(1), 20.

Johnson, S. Y., S. R. Hartwell, and P. Dartnell (2014), Offset of latest Pleistocene shoreface reveals slip rate on the Hosgri strike-slip fault, offshore central California, *Bull. Seismol. Soc. Am.*, *104*(4), 1650–1662.

Kaizuka, S., T. Matsuda, M. Nogami, and N. Yonekura (1973), Quaternary tectonic and recent seismic crustal movements in the Arauco peninsula and its environs, central Chile, *Geographical Reports of Tokyo Metropolitan University*, *8*, 1–49.

Kitamura, A., M. Koyama, K. Itasaka, Y. Miyairi, and H. Mori (2014), Abrupt late Holocene uplifts of the southern Izu Peninsula, central Japan: Evidence from emerged marine sessile assemblages, *Island Arc*, *23*(1), 51–61.

Kodaira, S., T. No, Y. Nakamura, T. Fujiwara, Y. Kaiho, S. Miura, N. Takahashi, Y. Kaneda, and A. Taira (2012), Coseismic fault rupture at the trench axis during the 2011 Tohoku-oki earthquake, *Nat. Geosci.*, *5*(9), 646–650.

Komar, P. D. (1998), *Beach Processes and Sedimentation*, 546 pp., Prentice-Hall, N. J.

Lajoie, K. R. (1986), *Coastal Tectonics: Active Tectonics*, pp. 95–124, Natl. Acad. Press, Washington, D. C.

Lange, D., et al. (2012), Aftershock seismicity of the 27 February 2010 M_w 8.8 Maule earthquake rupture zone, *Earth Planet. Sci. Lett.*, *317–318*(0), 413–425.

Lavenu, A., and J. Cembrano (1999), Compressional-and transpressional-stress pattern for Pliocene and Quaternary brittle deformation in fore arc and intra-arc zones (Andes of central and southern Chile), *J. Struct. Geol.*, *21*(12), 1669–1691.

Leclerc, F., N. Feuillet, M. Perret, G. Cabioch, S. Bazin, J.-F. Lebrun, and J. Saurel (2015), The reef platform of Martinique: Interplay between eustasy, tectonic subsidence and volcanism since late Pleistocene, *Mar. Geol.*, *369*, 34–51.

Leymerie, A. (1841), *Suite du mémoire sur le terrain crétacé du département de l'Aube*, Memoir 4, 34 pp., Langlois et Leclercq, Paris.

Li, S., M. Moreno, M. Rosenau, D. Melnick, and O. Oncken (2014), Splay fault triggering by great subduction earthquakes inferred from finite element models, *Geophys. Res. Lett.*, *41*, 385–391, doi:10.1002/2013GL058598.

Liberty, L. M., S. P. Finn, P. J. Haeussler, T. L. Pratt, and A. Peterson (2013), Megathrust splay faults at the focus of the Prince William Sound asperity, Alaska, *J. Geophys. Res. Solid Earth*, *118*, 5428–5441.

Lieser, K., I. Grevemeyer, D. Lange, E. Flueh, F. Tilmann, and E. Contreras-Reyes (2014), Splay fault activity revealed by aftershocks of the 2010 M_w 8.8 Maule earthquake, central Chile, *Geology*, *42*(9), 823–826.

Lin, Y.-N., et al. (2013), Coseismic and postseismic slip associated with the 2010 Maule earthquake, Chile: Characterizing the Arauco Peninsula barrier effect, *J. Geophys. Res. Solid Earth*, *118*, 3142–3159, doi:10.1002/jgrb.50207.

Lomnitz, C. (2004), Major earthquakes of Chile: A historical survey, 1535–1960, *Seismol. Res. Lett.*, *75*(3), 368–378.

Loveless, J. P., R. W. Allmendinger, M. E. Pritchard, and G. González (2010), Normal and reverse faulting driven by the subduction zone earthquake cycle in the northern Chilean fore arc, *Tectonics*, *29*, TC2001, doi:10.1029/2009TC002465.

Luján, M., A. Crespo-Blanc, and M. Comas (2011), Morphology and structure of the Camarinal sill from high-resolution bathymetry: Evidence of fault zones in the Gibraltar Strait, *Geo Mar. Lett.*, *31*(3), 163–174.

Melnick, D. (2016), Rise of the central Andean coast by earthquakes straddling the Moho, *Nat. Geosci.*, *9*(5), 401–407.

Melnick, D., B. Bookhagen, H. Echtler, and M. Strecker (2006), Coastal deformation and great subduction earthquakes, Isla Santa María, Chile (37°S), *Geol. Soc. Am. Bull.*, *118*(11/12), 1463–1480.

Melnick, D., B. Bookhagen, M. R. Strecker, and H. P. Echtler (2009), Segmentation of megathrust rupture zones from fore-arc deformation patterns over hundreds to millions of years, Arauco peninsula, Chile, *J. Geophys. Res.*, *114*, B01407, doi:10.1029/2008JB005788.

Melnick, D., and H. P. Echtler (2006), Inversion of forearc basins in south-central Chile caused by rapid glacial age trench fill, *Geology*, *34*(9), 709–712.

Melnick, D., M. Moreno, M. Cisternas, and A. s. Tassara (2012a), Darwin seismic gap closed by the 2010 Maule earthquake, *Andean Geol.*, *39*(3), 558–563.

Melnick, D., M. Moreno, M. Motagh, M. Cisternas, and R. L. Wesson (2012b), Splay fault slip during the M_w 8.8 2010 Maule Chile earthquake, *Geology*, *40*(3), 251–254.

Melnick, D., M. Moreno, M. Motagh, M. Cisternas, and R. L. Wesson (2013), Splay fault slip during the M_w 8.8 2010 Maule Chile earthquake: REPLY, *Geology*, *41*(12), e310–e310.

Moore, G., N. Bangs, A. Taira, S. Kuramoto, E. Pangborn, and H. Tobin (2007), Three-dimensional splay fault geometry and implications for tsunami generation, *Science*, *318*(5853), 1128–1131.

Moore, J. C. (1979), Variation in strain and strain rate during underthrusting of trench deposits, *Geology*, *7*(4), 185–188.

Moreno, M., J. Klotz, D. Melnick, H. Echtler, and K. Bataille (2008), Active faulting and heterogeneous deformation across a megathrust segment boundary from GPS data, south central Chile (36–39°S), *Geochem. Geophys. Geosyst.*, *9*, Q12024, doi:10.1029/2008GC002198.

Moreno, M., D. Melnick, M. Rosenau, J. Baez, J. Klotz, O. Oncken, A. Tassara, J. Chen, K. Bataille, and M. Bevis (2012), Toward understanding tectonic control on the M_w 8.8 2010 Maule Chile earthquake, *Earth Planet. Sci. Lett.*, *321*, 152–165.

Moreno, M., M. Rosenau, and O. Oncken (2010), 2010 Maule earthquake slip correlates with pre-seismic locking of Andean subduction zone, *Nature*, *467*(7312), 198–202.

Morris, A., D. A. Ferrill, and D. B. Henderson (1996), Slip-tendency analysis and fault reactivation, *Geology*, *24*(3), 275–278.

Mountjoy, J. J., and P. M. Barnes (2011), Active upper plate thrust faulting in regions of low plate interface coupling, repeated slow slip events, and coastal uplift: Example from the Hikurangi Margin, New Zealand, *Geochem. Geophys. Geosyst.*, *12*, Q01005, doi:10.1029/2010GC003326.

Mukoyoshi, H., A. Sakaguchi, K. Otsuki, T. Hirono, and W. Soh (2006), Co-seismic frictional melting along an out-of-sequence thrust in the Shimanto accretionary complex. Implications on the tsunamigenic potential of splay faults in modern subduction zones, *Earth Planet. Sci. Lett.*, *245*(1), 330–343.

Nakamura, T., and T. Nakamori (2007), A geochemical model for coral reef formation, *Coral Reefs*, *26*(4), 741–755.

Okada, Y. (1985), Surface deformation due to shear and tensile faults in a half-space, *Bull. Seismol. Soc. Am.*, *75*(4), 1135–1154.

Papazachos, B., E. Scordilis, D. Panagiotopoulos, C. Papazachos, and G. Karakaisis (2004), Global relations between seismic fault parameters and moment magnitude of earthquakes, *Bull. Geol. Soc. Greece*, *36*, 1482–1489.

Park, J.-O., T. Tsuru, S. Kodaira, P. R. Cummins, and Y. Kaneda (2002), Splay fault branching along the Nankai subduction zone, *Science*, *297*(5584), 1157–1160.

Paskoff, R. P. (1977), Quaternary of Chile: The state of research, *Quatern. Res.*, *8*(1), 2–31.

Pedoja, K., L. Husson, M. E. Johnson, D. Melnick, C. Witt, S. Pochat, M. I. Nexer, B. Delcaillau, T. Pinegina, and Y. Poprawski (2014), Coastal staircase sequences reflecting sea-level oscillations and tectonic uplift during the Quaternary and Neogene, *Earth Sci. Rev.*, *132*, 13–38.

Perry, C. T. (1996), Distribution and abundance of macroborers in an upper Miocene reef system, Mallorca, Spain: Implications for reef development and framework destruction, *Palaios*, *11*, 40–56.

Plafker, G. (1967), Surface faults on Montague Island associated with the 1964 Alaska earthquake, *U.S. Geol. Surv. Prof. Pap.*, *543–G*, p. 42.

Pleydell, S., and B. Jones (1988), Boring of various faunal elements in the Oligocene-Miocene Bluff Formation of Grand Cayman, British West Indies, *J. Paleo.*, *62*(03), 348–367.

Refice, A., E. Giachetta, and D. Capolongo (2012), SIGNUM: A Matlab, TIN-based landscape evolution model, *Comput. Geosci.*, *45*, 293–303.

Regard, V., M. Saillard, J. Martinod, L. Audin, S. b. Carretier, K. Pedoja, R. Riquelme, P. Paredes, and G. Hérail (2010), Renewed uplift of the central Andes Forearc revealed by coastal evolution during the Quaternary, *Earth Planet. Sci. Lett.*, *297*(1), 199–210.

Rietbrock, A., and F. Waldhauser (2004), A narrowly spaced double-seismic zone in the subducting Nazca plate, *Geophys. Res. Lett.*, *31*, L10608, doi:10.1029/2004GL019610.

Rohling, E., K. Grant, M. Bolshaw, A. Roberts, M. Siddall, C. Hemleben, and M. Kucera (2009), Antarctic temperature and global sea level closely coupled over the past five glacial cycles, *Nat. Geosci.*, *2*(7), 500–504.

Ryder, I., A. Rietbrock, K. Kelson, R. Bürgmann, M. Floyd, A. Socquet, C. Vigny, and D. Carrizo (2012), Large extensional aftershocks in the continental forearc triggered by the 2010 Maule earthquake, Chile, *Geophys. J. Int.*, *188*(3), 879–890.

Sakaguchi, A., F. Chester, D. Curewitz, O. Fabbri, D. Goldsby, G. Kimura, C.-F. Li, Y. Masaki, E. J. Screaton, and A. Tsutsumi (2011), Seismic slip propagation to the updip end of plate boundary subduction interface faults: Vitrinite reflectance geothermometry on Integrated Ocean Drilling Program NanTro SEIZE cores, *Geology*, *39*(4), 395–398.

Satake, K., Y. Fujii, T. Harada, and Y. Namegaya (2013), Time and space distribution of coseismic slip of the 2011 Tohoku earthquake as inferred from tsunami waveform data, *Bull. Seismol. Soc. Am.*, *103*(2B), 1473–1492.

Savage, J. (1983), A dislocation model of strain accumulation and release at a subduction zone, *J. Geophys. Res.*, *88*(B6), 4984–4996.

Schurr, B., G. n. Asch, S. Hainzl, J. Bedford, A. Hoechner, M. Palo, R. Wang, M. Moreno, M. Bartsch, and Y. Zhang (2014), Gradual unlocking of plate boundary controlled initiation of the 2014 Iquique earthquake, *Nature*, *512*(7514), 299–302.

Shackleton, N. J. (2000), The 100,000-year ice-age cycle identified and found to lag temperature, carbon dioxide, and orbital eccentricity, *Science*, *289*(5486), 1897–1902.

Sherman, C., C. Fletcher, and K. Rubin (1999), Marine and meteoric diagenesis of Pleistocene carbonates from a nearshore submarine terrace, Oahu, Hawaii, *J. Sediment. Res.*, *69*(5).

Shikakura, Y. (2014), Marine terraces caused by fast steady uplift and small coseismic uplift and the time-predictable model: Case of Kikai Island, Ryukyu Islands, Japan, *Earth Planet. Sci. Lett.*, *404*, 232–237.

Shirzaei, M., R. Bürgmann, O. Oncken, T. Walter, P. Victor, and O. Ewiak (2012), Response of forearc crustal faults to the megathrust earthquake cycle: InSAR evidence from Mejillones Peninsula, northern Chile, *Earth Planet. Sci. Lett.*, *333*, 157–164.

Servicio Hidrográfico y Oceanográfico de la Armada de Chile (2004), Golfo de Arauco in 6120, ed., Cartas nauticas Digitales: Santiago, Servicio Hidrografico y Oceanografico de la Armada de Chile.

Sibson, R. H. (1985), A note on fault reactivation, *J. Struct. Geol.*, *7*(6), 751–754.

Siddall, M., E. Rohling, W. G. Thompson, and C. Waelbroeck (2008), Marine isotope stage 3 sea level fluctuations: Data synthesis and new outlook, *Rev. Geophys.*, *46*, RG4003, doi:10.1029/2007RG000226.

Siddall, M., E. J. Rohling, A. Almogi-Labin, C. Hemleben, D. Meischner, I. Schmelzer, and D. Smeed (2003), Sea-level fluctuations during the last glacial cycle, *Nature*, *423*(6942), 853–858.

Singh, S., N. Hananto, and A. Chauhan (2011), Enhanced reflectivity of backthrusts in the recent great Sumatran earthquake rupture zones, *Geophys. Res. Lett.*, *38*, L04302, doi:10.1029/2010GL046227.

Storms, J. E., and D. J. P. Swift (2003), Shallow-marine sequences as the building blocks of stratigraphy: Insights from numerical modelling, *Basin Res.*, *15*, 287–303.

Sunamura, T. (1992), *Geomorphology of Rocky Coasts*, 302 pp., John Wiley, New York.

Swann, G. E., A. W. Mackay, M. J. Leng, and F. Demory (2005), Climatic change in central Asia during MIS 3/2: A case study using biological responses from Lake Baikal, *Global Planet. Change*, *46*(1), 235–253.

ten Brink, U. S., J. Song, and R. C. Bucknam (2006), Rupture models for the AD 900–930 Seattle fault earthquake from uplifted shorelines, *Geology*, *34*(7), 585–588.

Thébaudeau, B., A. S. Trenhaile, and R. J. Edwards (2013), Modelling the development of rocky shoreline profiles along the northern coast of Ireland, *Geomorphology*, *203*, 66–78.

Toda, S., and H. Tsutsumi (2013), Simultaneous reactivation of two, subparallel, inland normal faults during the M_w 6.6 11 April 2011 Iwaki earthquake triggered by the M_w 9.0 Tohoku-oki, Japan, earthquake, *Bull. Seismol. Soc. Am.*, *103*(2B), 1584–1602.

Tong, X., D. Sandwell, K. Luttrell, B. Brooks, M. Bevis, M. Shimada, J. Foster, R. Smalley, H. Parra, and J. C. Báez Soto (2010), The 2010 Maule, Chile earthquake: Downdip rupture limit revealed by space geodesy, *Geophys. Res. Lett.*, *37*, L24311, doi:10.1029/2010GL045805.

Twidale, C., J. Bourne, and J. V. Romani (2005), Beach etching and shore platforms, *Geomorphology*, *67*(1), 47–61.

Victor, P., M. Sobiesiak, J. Glodny, S. N. Nielsen, and O. Oncken (2011), Long-term persistence of subduction earthquake segment boundaries: Evidence from Mejillones Peninsula, northern Chile, *J. Geophys. Res.*, *116*, B02402, doi:10.1029/2010JB007771.

von Huene, R., J. J. Miller, D. Klaeschen, and P. Dartnell (2016), A possible source mechanism of the 1946 Unimak Alaska far-field tsunami: Uplift of the mid-slope terrace above a splay fault zone, *Pure Appl. Geophys.*, *173*(12), 4189–4201.

Waldhauser, F. (2001), HypoDD-A program to compute double-difference hypocenter locations, 2331–1258.

Waldhauser, F., and W. L. Ellsworth (2000), A double-difference earthquake location algorithm: Method and application to the northern Hayward fault, California, *Bull. Seismol. Soc. Am.*, *90*(6), 1353–1368.

Waldhauser, F., D. P. Schaff, T. Diehl, and E. R. Engdahl (2012), Splay faults imaged by fluid-driven aftershocks of the 2004 M_w 9.2 Sumatra-Andaman earthquake, *Geology*, *40*(3), 243–246.

Wang, K., and Y. Hu (2006), Accretionary prisms in subduction earthquake cycles: The theory of dynamic Coulomb wedge, *J. Geophys. Res.*, *111*, doi:10.1029/2005JB004094.

Wells, D. L., and K. J. Coppersmith (1994), New empirical relationships among magnitude, rupture length, rupture width, rupture area, and surface displacement, *Bull. Seismol. Soc. Am.*, *84*(4), 974–1002.

Wells, R. E., R. J. Blakely, Y. Sugiyama, D. W. Scholl, and P. A. Dinterman (2003), Basin-centered asperities in great subduction zone earthquakes: A link between slip, subsidence, and subduction erosion?, *J. Geophys. Res.*, *108*(B10), 2507, doi:10.1029/2002JB002072.

Wendt, J., D. D. Oglesby, and E. L. Geist (2009), Tsunamis and splay fault dynamics, *Geophys. Res. Lett.*, *36*, L15303, doi:10.1029/2009GL038295.

Wenzel, G., J. Wathelet, G. Slighta, and O. Vigneras (1975), Mapas de minas de carbon de la octava region.: Concepcion, ENACAR, p. 7.

Wesson, R. L., D. Melnick, M. Cisternas, M. Moreno, and L. L. Ely (2015), Vertical deformation through a complete seismic cycle at Isla Santa Maria, Chile, *Nat. Geosci.*, *8*(7), 547–551.

Whittaker, J. C. (2010), *Flintknapping: Making and Understanding Stone Tools*, 352 pp., Univ. of Tex. Press, Austin.